

1 **Enhancing Phase Identification in Waste-to-Energy Fly Ashes: Role of Raman**
2 **Spectroscopy, Background Fluorescence, and Photobleaching**

3

4 Hamza Samouh, Vikram Kumar, Halle-Mari Santiago, Nishant Garg

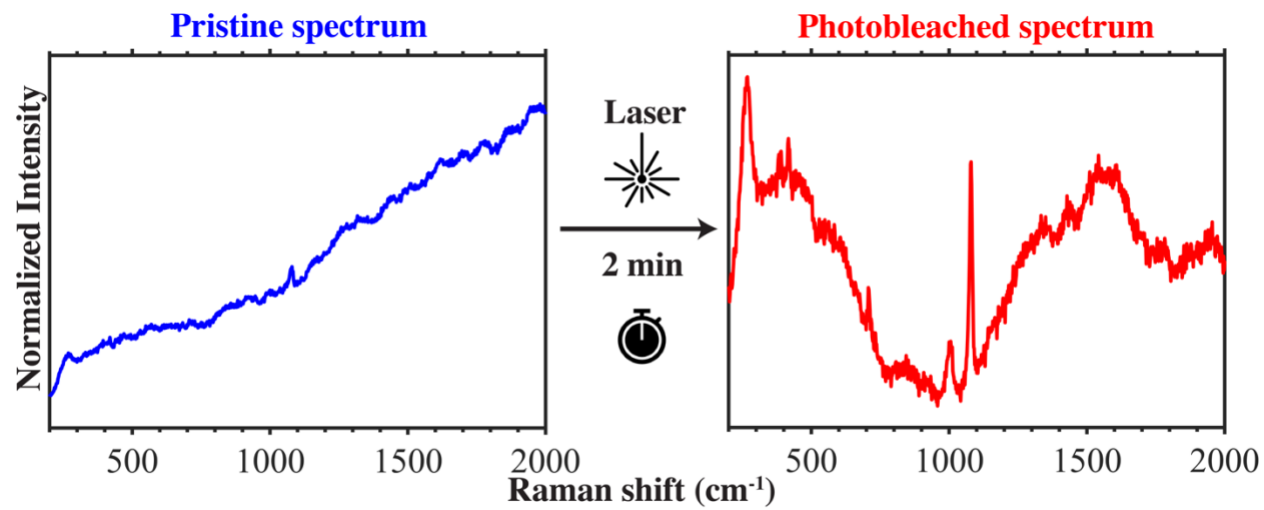
5 Department of Civil and Environmental Engineering, University of Illinois Urbana-Champaign,

6 Urbana, Illinois, 61801, United States

7

8 **Graphical Abstract**

9



10

11 **Abstract**

12

13 Waste-to-Energy (WTE) facilities incinerate ~11% (~ 222 Mt) of global solid waste, generating
14 bottom and fly ashes. Landfilling these ashes is costly, and risks releasing contaminants into the
15 environment. Instead, using WTE ashes in secondary industrial applications can circumvent such
16 environmental risks. However, their secondary use is restricted by their inconsistent mineralogy,
17 which may vary due to fluctuating waste composition and combustion conditions. Therefore, there
18 is a need for rapid and reliable monitoring of WTE fly ash mineralogy. Here, we evaluate the
19 employment of Raman spectroscopy for that purpose. Our initial investigation of 12 unique WTE
20 fly ashes resulted in excessive fluorescence, rendering key Raman peaks obscure. To address this
21 issue, we report that a mere 2 minutes of photobleaching can significantly reduce this fluorescence,
22 facilitating the detection of calcite, calcium sulfate, zincite, and carbon – phases previously
23 undetectable in original spectra. These results show the potential of Raman spectroscopy for rapid
24 monitoring of WTE fly ash mineralogy, which could be beneficial in diverting these ashes from
25 landfill.

26

27 **Keywords**

28

29 Waste-to-Energy, WTE fly ash, Raman Spectroscopy, Photobleaching, Photolysis

30

31

32

33

34

35

36 **Environmental Implication**

37 Incineration for energy recovery is a key component of waste management. After incineration,
38 hazardous heavy metals are concentrated in the waste-to-energy (WTE) fly ash residues. The WTE
39 fly ash residues are generally landfilled, where they risk contaminating the natural environment.
40 These risks can be avoided by diverting WTE fly ashes from landfills to composition-dependent
41 upcycling avenues. In this study, we demonstrated Raman spectroscopy as a potential method to
42 elucidate the mineralogical characteristics of WTE fly ashes in a rapid and reliable manner.
43 Understanding the chemical characteristics of WTE fly ashes is essential to diverting them from
44 landfills to composition-dependent upcycling pathways.

45

46 **1. Introduction**

47 Global waste generation in 2015 stood at 1.99 Gt and is projected to increase to 3.53 Gt by 2050.^{1,2}
48 Such a significant increase in waste generation, especially in densely populated regions of the
49 world, will likely make waste management increasingly reliant on Waste-to-Energy (WTE).³
50 Incineration at WTE facilities reduces the weight and volume of solid waste by 70-80 % and 90
51 %, respectively, while generating steam and electricity.⁴ The weight and volume of solid waste
52 thus reduced is advantageous because of the limited availability of landfilling space in various
53 parts of the US.⁵ However, the residual solid waste fraction left after incineration is in the form of
54 complex WTE bottom and fly ashes. WTE bottom ashes contain significant proportions of ferrous
55 and non-ferrous metals. Therefore, iron and aluminum are usually recovered from WTE bottom
56 ashes through magnetic and eddy current separations.⁶ The WTE bottom ash fraction remaining
57 after metal extraction is either landfilled or used as an aggregate, a supplementary cementitious
58 material (SCM), or raw material for cement production.⁷⁻¹² Unlike WTE bottom ashes, WTE fly
59 ashes are concentrated with volatile metals, such as Cd, Pb, and Zn.^{13,14} These metals make WTE
60 fly ashes hazardous. Therefore, from a management standpoint, WTE fly ashes are usually
61 landfilled after chemical stabilization.¹⁵ However, recent studies have demonstrated that WTE fly
62 ashes can be used as SCMs.^{16,17} When employed as SCMs, WTE fly ashes do not merely act as
63 fillers; they may also influence the early-age mechanical behavior of
64 concrete.^[NO_PRINTED_FORM]¹⁸ For instance, ZnO in WTE fly ashes, if present, can retard
65 cement hydration considerably and thus subsequently affect the mechanical properties of
66 cementitious materials.¹⁹ These mechanical properties change depending on the chemical
67 (elemental and mineralogical composition) and physical (particle size) characteristics of WTE fly
68 ashes.²⁰ Specifically, the chemical composition of WTE fly ashes is known to vary widely.²¹⁻²³ As

69 a result, the properties of a cementitious material employing WTE fly ashes can show significant
70 variation.

71
72 The variability in WTE fly ash composition stems from irregular waste composition and
73 combustion environment.⁴ These parameters affect the thermal and chemical characteristics of
74 solid waste, influencing the elemental partitioning between WTE bottom and fly ashes.²⁴⁻²⁶
75 Generally, elements such as S, Br, Cl, F, Cd, Hg, Pb, Sb, Sn, Cu, and Zn are preferentially
76 partitioned to the flue gas because of evaporation. Advanced air pollution control systems
77 comprising cyclones, electrostatic precipitators, bag filters, and semi-dry or wet scrubber systems
78 remove preferentially partitioned elements by injecting an adsorbent, mostly lime, in the flue gas.⁴
79 The added lime reacts with Cl and S present as HCl (g) and SO₂ (g) in the flue gas. HCl (g) in the
80 flue gas reacts with lime to form calcium chloride hydroxide (CaClOH) or calcium chloride
81 (CaCl₂).²⁷⁻²⁹ Similarly, the SO₂ (g) in the flue gas reacts with lime to form gypsum (CaSO₄·2H₂O).⁴
82 In addition to these principal reactions, reactions amongst other elements in the flue gas may occur.
83 Such reactions result in the formation of minor phases, such as CuCO₃, Cu(OH)₂, CuO, CuS,
84 CuCl₂, Cu₂O, ZnFe₂O₄, Zn₄Si₂O₇, ZnAl₂O₄, ZnO, Zn(OH)₂, ZnCl₂, and Zn₅(CO₃)₂(OH)₂.³⁰⁻³⁴
85 Finally, elements such as Si, Fe, Al, Na, and K can also be present in the flue gas because of
86 entrainment. These elements may be present as inert minerals or react with other elements in the
87 flue gas to form additional compounds, such as quartz (SiO₂), gehlenite (Ca₂Al(AlSi)O₇), halite
88 (NaCl), sylvite (KCl), and hydrocalumite (Ca₂Al(OH)₆Cl(H₂O)₂).²⁰ In summary, the elements in
89 the flue gas react amongst themselves or with injected lime to form numerous phases. These
90 multiple phases formed during the air pollution control dictate the chemical properties of air
91 pollution control residues, also referred to as WTE fly ashes. The chemical properties of WTE fly

92 ashes thus formed are likely time-dependent because waste composition may show temporal
93 variation. Therefore, to establish WTE fly ashes as reliable SCMs or any other useful industrial
94 byproduct, monitoring their chemical characteristics (both elemental and mineralogical) in real-
95 time would be advantageous for ash management.

96
97 The elemental composition of WTE ashes is usually obtained from X-ray fluorescence (XRF),
98 whereas the mineralogical characteristics are evaluated with powder X-ray diffraction (XRD).¹⁸
99 With XRF, the elemental composition of WTE fly ashes can be obtained rapidly (within minutes),
100 whereas the application of XRD for evaluating the mineralogical characteristics is not rapid.³⁵
101 Hence, there is a need to employ alternate characterization techniques to assess the mineralogical
102 characteristics of WTE fly ashes rapidly. Raman spectroscopy could be a promising technique to
103 fast monitor the mineralogical characteristics of WTE fly ashes. This technique exploits the
104 molecular vibrational characteristics (changes in polarizability) to distinguish between different
105 mineralogical species.³⁶ Apart from being rapid, this technique can provide insights that
106 complement the information obtained from X-ray diffraction. For example, overlaps between the
107 Bragg reflections of crystalline phases in the powder X-ray diffraction pattern of WTE fly ashes
108 limit our ability to identify minor mineralogical species in WTE fly ashes. In such cases, the
109 complementary information from Raman spectroscopy can help identify minor mineralogical
110 species.

111
112 In the recent past, Raman spectroscopy and imaging have been used to study various static and
113 dynamic systems, such as microplastics, carcinogens, and cement.³⁶⁻⁴¹ However, its application
114 to WTE fly ashes is not straightforward. First, as part of the air pollution control, activated carbon

115 is injected to remove Hg, Cd, Tl, and As from the flue gas.⁴ The carbon thus injected becomes a
116 component of the WTE fly ashes. The presence of such organic species is well known to cause
117 fluorescence and obscure any meaningful interpretation of the Raman signal.⁴² Second, WTE fly
118 ashes contain phases, such as CaClOH, for which the characteristic Raman peaks are unknown. In
119 this article, we overcome these limitations by first successfully reducing fluorescence by
120 photobleaching, i.e., premature irradiation to the laser. By systematically studying 12 unique WTE
121 fly ashes, we show that a mere 2 minutes of photobleaching causes a significant reduction in
122 fluorescence, enabling the identification of key mineral phases such as calcite, calcium sulfate,
123 zincite, and carbon in WTE fly ashes. Second, we synthesize pure CaClOH and report its
124 characteristic Raman peaks, which are useful in detecting and assigning this phase. Finally, we
125 demonstrate that commonly occurring phases in WTE fly ashes – calcite, calcium sulfate, zincite,
126 and calcium chloride hydroxide – are not susceptible to photobleaching-led photolysis. Thus,
127 photobleaching can reduce background fluorescence in Raman spectra while not causing a
128 significant reduction in the characteristic Raman peak intensity of key phases. These results
129 suggest that Raman spectroscopy can successfully monitor the mineralogical characteristics of
130 WTE fly ashes.

131

132 **2. Materials and Methods**

133 **2.1. Materials**

134 This paper investigates 12 unique WTE fly ashes obtained at different times from a mass-burn
135 waste-to-energy facility in the United States. The WTE facility employed lime for acid-gas
136 abatement. Therefore, the WTE fly ashes in this study are rich in calcium. Furthermore, Raman

137 spectroscopy indicated the presence of calcite, calcium sulfate, and zincite in WTE fly ashes. A
138 commonly occurring phase in WTE fly ashes whose characteristic Raman signals are unknown is
139 calcium chloride hydroxide (CaClOH). These four phases may disintegrate when photobleached
140 because of photolysis. So, the influence of photobleaching on these phases was evaluated further.
141 For this purpose, reagent grade calcite (powder size $\leq 50\mu\text{m}$, 98 %, Sigma Aldrich), zincite (Arcos
142 Organics, ACS Reagent), and calcium sulfate (Drierite) were used. Finally, pure CaClOH was
143 synthesized by modifying a previously reported protocol for synthesizing hydroxide halides;^{43,44}
144 specifically, equimolar amounts of calcium hydroxide (Arcos Organics, 98 % pure) and calcium
145 chloride (Sigma Aldrich, 93 % pure) heated in a furnace at 337 °C for seven days yielded pure
146 CaClOH. The furnace was intermittently flushed with Argon gas to minimize the carbonation of
147 calcium hydroxide and calcium chloride hydroxide.

148 **2.2. Experimental Methods**

149 **X-ray Fluorescence**

150 The elemental composition of WTE fly ashes was determined through X-Ray Fluorescence (XRF)
151 on a Shimadzu EDX-7000 spectrometer employing a Rhodium anode as an X-ray source. The
152 powdered WTE fly ash specimens ($< 45 \mu\text{m}$) were transferred to a sample cell covered with an
153 ultralene film. After that, the XRF spectra were collected between 0-40 keV in the presence of
154 Helium. The fluorescence spectra thus collected were processed to determine elemental
155 concentrations based on the Fundamental Parameter algorithm.⁴⁵

156 **X-ray Diffraction**

157 The powder X-Ray Diffraction (XRD) patterns of pure phases and WTE fly ashes were collected
158 on powder specimens finer than 45 μm on a Bruker D8 Advance diffractometer (40 kV and 40
159 mA) with Cu $K\alpha$ radiation ($\lambda=1.5418 \text{ \AA}$). The diffractometer operated in the Bragg-Brentano
160 focusing configuration ($\theta - 2\theta$ configuration). A detailed description of the diffractometer X-ray
161 optics is described elsewhere.²⁰ In this study, diffraction patterns were collected between 10° and
162 $70^\circ 2\theta$ at a step size and step time of 0.01° and 0.15 seconds, respectively. Finally, the minerals in
163 pure phases and WTE fly ashes were identified by comparing the collected powder diffraction
164 patterns with the diffraction patterns of pure phases in the International Center for Diffraction Data
165 Powder Diffraction File database.

166 **Raman Spectroscopy**

167 All the Raman spectroscopy experiments were performed on the HORIBA MacroRAM
168 spectrometer. The spectrometer directs a 785 nm excitation laser on the sample, and the photons
169 thus emitted are collected in the backscattered direction and filtered using an edge filter. The
170 backscattered photons collected are then dispersed with a fixed spectrograph (holographic grating
171 with a groove density of 685 gr/mm) and detected with a thermoelectrically cooled (-50°C)
172 Syncerity near-IR back-illuminated CCD camera. This configuration allows Raman signal
173 (Stokes) collection between 100 and 3400 cm^{-1} . Several factors, such as particle size distribution,
174 sample thickness, surface roughness, and apparent density, influence the Raman signal of
175 powdered specimens.⁴⁶⁻⁵⁰ Therefore, for consistency, Raman spectra were acquired on tablets
176 prepared from pellet pressing of powdered specimens finer than $45 \mu\text{m}$ in size. The tablet prepared
177 through the pellet pressing process is circular (7 mm diameter) and has a smooth flat surface. An
178 area $\sim 90 \times 140 \mu\text{m}$ in size on the tablet is exposed to the 785 nm excitation laser under variable

179 conditions. In this study, the Raman signal of each tablet specimen is collected by changing three
180 parameters – the acquisition time, time of pre-exposure, and the laser power.

181
182 For WTE fly ash specimens, the Raman signal was obtained with a fixed acquisition time of 6
183 seconds, whereas the Raman signal of pure phases was collected with a fixed acquisition time of
184 1 second. These acquisition times were selected through exploratory measurements to maximize
185 the signal-to-noise ratio. The second laser parameter, i.e., the pre-exposure time, was varied to
186 study photobleaching. Specifically, the Raman signal was collected after 0, 1, 2, 5, 10, 20, and 30
187 minutes of pre-exposure. Finally, the effect of laser power on the Raman signal was studied by
188 collecting Raman spectra at 10, 30, 50, 70, and 90 % laser power. The laser power scales linearly,
189 and 100 % laser power corresponds to 450 mW.

190 **Raman Imaging**

191 Raman hyperspectral imaging was performed on a pellet (7 mm in diameter) prepared from a
192 powdered ash specimen with a WITec Alpha 300 series SNOM microscope. The Raman
193 hyperspectral data was collected with a 785 nm excitation laser using a 20x objective at an
194 excitation power of 20 mW and a 600 g/mm grating coupled to a CCD camera. Specifically, 3600
195 Raman spectra were collected on a 1 mm × 1 mm area (a grid of 80 by 80 points spaced 12.5 μm
196 apart) with an integration time of 1 s/point. Under these selected conditions, hyperspectral data
197 collection took ~2 hours. The collected hyperspectral data was further processed (Project FIVE
198 software) using true component analysis with external reference spectra (from RRUFF database)
199 to obtain the Raman phase maps.

200 **Thermogravimetric Analysis**

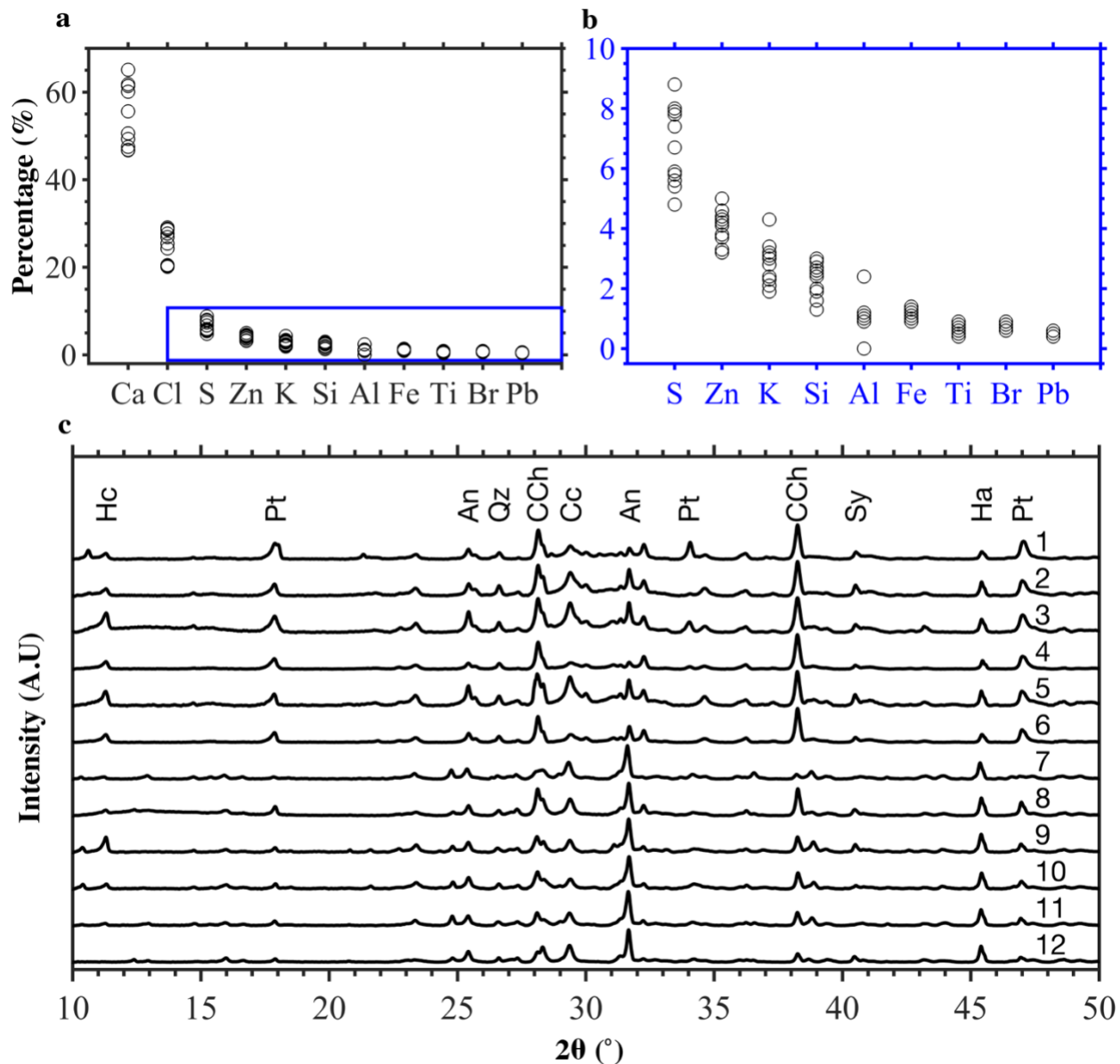
201 Thermogravimetric analyses were performed on a Q50 thermogravimetric analyzer from TA
202 instruments. 15-20 mg of powder specimens were heated from 20°C to 850°C at a heating rate of
203 20°C/min in the presence of nitrogen (flow rate = 60 ml/min). The obtained curves are presented
204 in Fig. S1 and S2.

205

206 **3. Results and Discussions**

207 **3.1. Elemental and Mineralogical Characterization of WTE Fly Ashes**

208 The elemental composition of WTE fly ashes investigated in this study (measured via XRF) is
209 depicted in Fig. 1a and 1b. Ca and Cl are the major elements in these WTE fly ashes. The remaining
210 elements that comprise the ash matrix in decreasing order of concentration are S, Zn, K, Si, Al, Fe,
211 Ti, Br, and Pb. These elements have been previously observed in WTE fly ashes.⁵¹ Ca in these
212 ashes comes from the lime used for flue gas deacidification, whereas the Cl in these ashes likely
213 comes from the plastics and chloride salts in the kitchen waste, i.e., NaCl.⁵² The speciation of the
214 elements in WTE fly ashes was investigated through powder-XRD. Diffraction patterns for all the
215 12 WTE fly ashes investigated in this study are illustrated in Fig. 1 c. From powder-XRD, we find
216 that Ca, Al, Cl, S, Si, K, and Na in the WTE fly ashes are present as hydrocalumite
217 ($\text{Ca}_2\text{Al}(\text{OH})_6\text{Cl}(\text{H}_2\text{O})_2$), portlandite ($\text{Ca}(\text{OH})_2$), anhydrite (CaSO_4), quartz (SiO_2), calcium
218 hydroxide chloride (CaClOH), calcite (CaCO_3), sylvite (KCl), and halite (NaCl). The speciation
219 of the remaining minor elements (Zn, Fe, Ti, Br, and Pb) could not be established through X-ray
220 powder diffraction. This is likely because the concentration of mineralogical species containing
221 these elements is low. The mineralogical species detected through powder-XRD here have been
222 noted to exist in WTE fly ashes in previous studies.^{53,54}



223

224 Fig. 1. Chemical composition of 12 unique WTE fly ashes analyzed in this study, where a and b show the
 225 elemental composition (weight %) of WTE fly ashes obtained via XRF, and c shows X-ray powder
 226 diffraction patterns. Phases corresponding to different diffraction peaks are indicated with the following
 227 abbreviations: Hc – Hydrocalumite ($\text{Ca}_2\text{Al}(\text{OH})_6\text{Cl}(\text{H}_2\text{O})_2$), Pt – Portlandite ($\text{Ca}(\text{OH})_2$), An – Calcium
 228 sulfate (Anhydrite, CaSO_4), Qz – Quartz (SiO_2), CCh – Calcium Chloride Hydroxide (CaClOH), Cc –
 229 Calcite (CaCO_3), Sy – Sylvite (KCl), Ha – Halite (NaCl).

230
 231
 232
 233
 234
 235
 236

237 **3.2. Photobleached Raman Spectra of WTE Fly Ashes**

238 **Identified Phases: Review and Collection of Raman Spectra**

239

240 The Raman spectra of all the phases present in WTE fly ashes except calcium chloride hydroxide

241 (identified via powder-XRD) are known. Hence, in this study, we synthesized pure calcium

242 chloride hydroxide in the lab, and collected its Raman spectrum (discussed in section 3.3). The

243 characteristic Raman peaks for all the phases identified through powder-XRD (including CaClOH)

244 are tabulated in Table 1. All the identified phases have characteristic Raman peaks. Therefore, the

245 phases identified through XRD should be, in principle, detectable via Raman spectroscopy. So, in

246 the next step, we collect the Raman spectrum of waste-to-energy fly ashes and attempt to identify

247 the Raman active phases in the WTE fly ashes.

248 *Table. 1. Characteristic Raman peaks for phases identified in the WTE fly ashes investigated in this study.*
 249 *The most prominent peak for a given phase is highlighted in bold.*

Phases	Raman Peaks (cm ⁻¹)	Reference
Hydrocalumite	271, 281, 296, 359, 397, 531, 704, 712, 1078, 1086 ; Reference reporting the Raman spectra of Hydrocalumite was collected on an impure specimen, consisting of calcite as an impurity.	Frost et al. ⁵⁵
Portlandite	252, 356, 680, 3620	Schmida et al. ⁵⁶
Calcium sulfate (Anhydrite)	235, 420, 503, 630, 678, 1017 , 1129, 1160	Ciobotă et al. ⁵⁷
Quartz	128, 205, 263, 354, 401, 463 , 697, 808, 1083, 1160, 1231	Chukanov et al. ⁵⁸
Calcium Chloride Hydroxide	142, 334, 669	This study
Calcite	156, 283, 713, 1086 , 1436, 1749, 1903, 2707, 2835, 2906	Edwards et al. ⁵⁹
Sylvite	Absence of first order Raman spectra; Second order Raman spectra is possible at 168, 200, and 350	Chukanov et al. ⁵⁸
Halite	Absence of first order Raman spectra; Second order Raman spectra is possible at 157, 176, 201, and 290	Chukanov et al. ⁵⁸
Rutile	142, 242, 441 , 611	Andò & Garzanti ⁶⁰

250

251 **Mitigating Fluorescence in WTE Fly Ashes via Photobleaching**

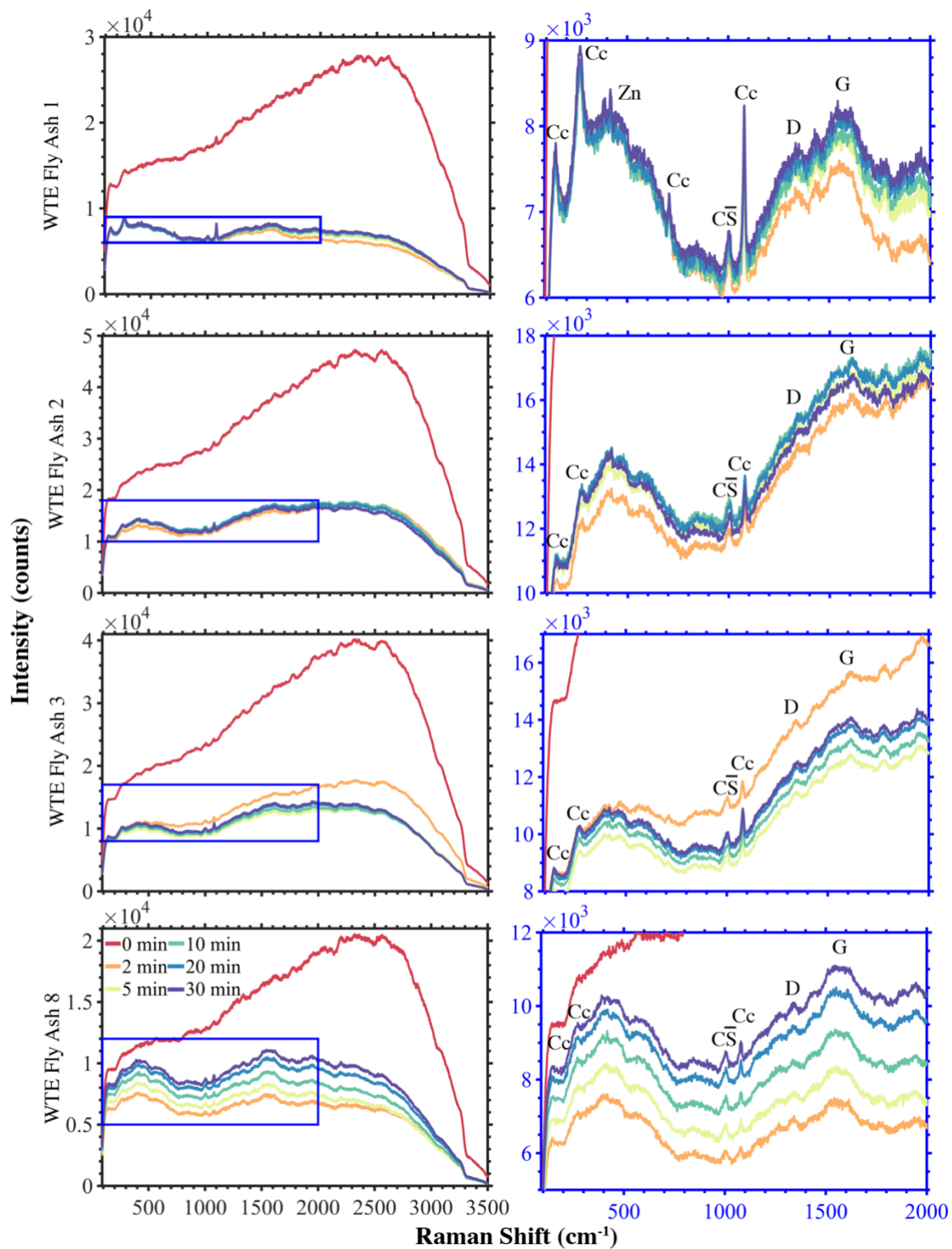
252 Initially, we selected four WTE fly ashes and collected their Raman spectra, which are depicted in

253 Fig. 2. For each ash, the Raman spectra were collected at a single spot (a spot size of 90 × 140 μm)

254 selected randomly, which may not be representative of a given ash specimen. However,
255 preliminary experiments on the WTE fly ash 1 specimen justified our selection of a single spot,
256 wherein we collected Raman spectra at 10 different spots (Fig. S5). The characteristic Raman
257 intensities show variation with spot location (Fig. S5). Nevertheless, we observe the occurrence of
258 similar Raman peaks for major phases irrespective of the spot location. Based on these preliminary
259 results, we collected the Raman spectrum for the remaining WTE fly ash specimens at a single
260 spot with an acquisition time of six seconds. The Raman spectra of the selected four WTE fly ash
261 specimens show excessive fluorescence (red-colored curves in Fig. 2), which obscures the
262 characteristic Raman peaks. Excessive fluorescence in the Raman signal of WTE fly ash
263 specimens may be caused by organic species present in WTE fly ashes.^{4,42} The observed
264 fluorescence in the Raman spectrum has been reported to be reduced by photobleaching in various
265 materials such as human skin tissue, rhodamine, bone tissue, human blood plasma, textiles,
266 chlorophylls, and carotenoids.⁶¹⁻⁶⁷ Hence, we attempt to reduce the fluorescence in the Raman
267 spectrum of four WTE fly ashes by photobleaching, i.e., pre-illumination of the sample with a
268 laser.

269
270 Herein, we observe a significant reduction in fluorescence for four WTE fly ashes photobleached
271 for 2, 5, 10, 20, and 30 minutes (Fig. 2). Because of reduced fluorescence, characteristic Raman
272 peaks become apparent. All the observed characteristic Raman peaks occur before 2000 cm^{-1} . So,
273 for better visualization of the characteristic Raman peaks, the Raman spectra are plotted in the
274 range $0\text{-}2000\text{ cm}^{-1}$ as depicted in Fig. 2. By observing the Raman spectrum of WTE fly ashes
275 photobleached for different intervals of time, we conclude that 2 minutes of photobleaching
276 suppresses the fluorescence adequately. Further increase in photobleaching time does not improve

277 the signal-to-noise ratio or add any further information to the Raman spectrum of WTE fly ashes
278 (Fig. 2). Another strategy to reduce fluorescence is to use longer laser wavelengths but we are
279 already employing 785 nm wavelength. However, on the flip side, longer wavelength lasers result
280 in a lower signal-to-noise ratio and this fact has been recently demonstrated for common
281 cementitious phases.⁵⁰



282

283 *Fig. 2. Raman spectra of WTE fly ashes before and after 0, 2, 5, 10, 20, and 30 minutes of photobleaching.*
 284 *All the Raman spectra in this figure were collected with an acquisition time of 6 seconds, and the laser*
 285 *power is fixed at 30 % (135 mW). The figures on the right magnify the area inside the blue rectangle of*
 286 *figures on the left. Cc denotes calcite, CS denotes calcium sulfate, Zn denotes zincite, D and G represent*
 287 *the carbon bands.*

288 **Detection of Characteristic Raman Peaks Post Photobleaching**

289 The characteristic Raman peaks at 1083 cm^{-1} and 1013 cm^{-1} , apparent after photobleaching, can
290 be assigned to calcite and calcium sulfate, respectively. Here, we note that in the literature,
291 hydrocalumite has been reported to show a characteristic Raman peak at 1083 cm^{-1} .⁵⁵ However,
292 the 1083 cm^{-1} Raman peak attributed to hydrocalumite likely belongs to calcite ($\nu_1(\text{CO}_3)^{2-}$
293 stretching), as the hydrocalumite characterized in the reference study consisted of calcite as an
294 impurity.⁵⁹ Our 1083 cm^{-1} Raman peak assignment to calcite is further validated by the absence
295 of the characteristic 531 cm^{-1} Raman peak belonging to hydrocalumite (Fig. 2 and Table 1).
296 Additionally, the observed 1017 cm^{-1} Raman peak is attributed to the S-O symmetric stretching
297 vibration in calcium sulfate.^{57,68} The characteristic Raman peaks for calcite and calcium sulfate
298 with varying intensities were detected in all four WTE fly ashes. Apart from the characteristic
299 Raman peaks of calcite and calcium sulfate, we notice an additional peak at 435 cm^{-1} for WTE Fly
300 Ash 1 (Fig. 2). The peak at 435 cm^{-1} suggests the presence of zincite (ZnO) in WTE fly ashes.⁶⁹
301 The presence of zincite in WTE fly ashes has been observed before with X-ray absorption near
302 edge structure (XANES).³⁴ Note that the characteristic Bragg reflections for zincite were not
303 identified in the powder-XRD patterns of WTE fly ashes likely because zincite is a minor
304 constituent in the WTE fly ashes. These observations suggest that Raman spectroscopy can shed
305 additional information on the mineralogy of WTE fly ashes after photobleaching.

306

307 As hypothesized, the photobleached Raman spectrum indicated the presence of organic species,
308 i.e., amorphous carbon, in WTE fly ashes. Specifically, in the photobleached Raman spectra, two
309 characteristic Raman bands corresponding to the graphite 'G' and disordered 'D' bands of
310 amorphous carbon are observed at 1350 cm^{-1} and 1600 cm^{-1} , respectively (Fig. 2).⁷⁰ These band

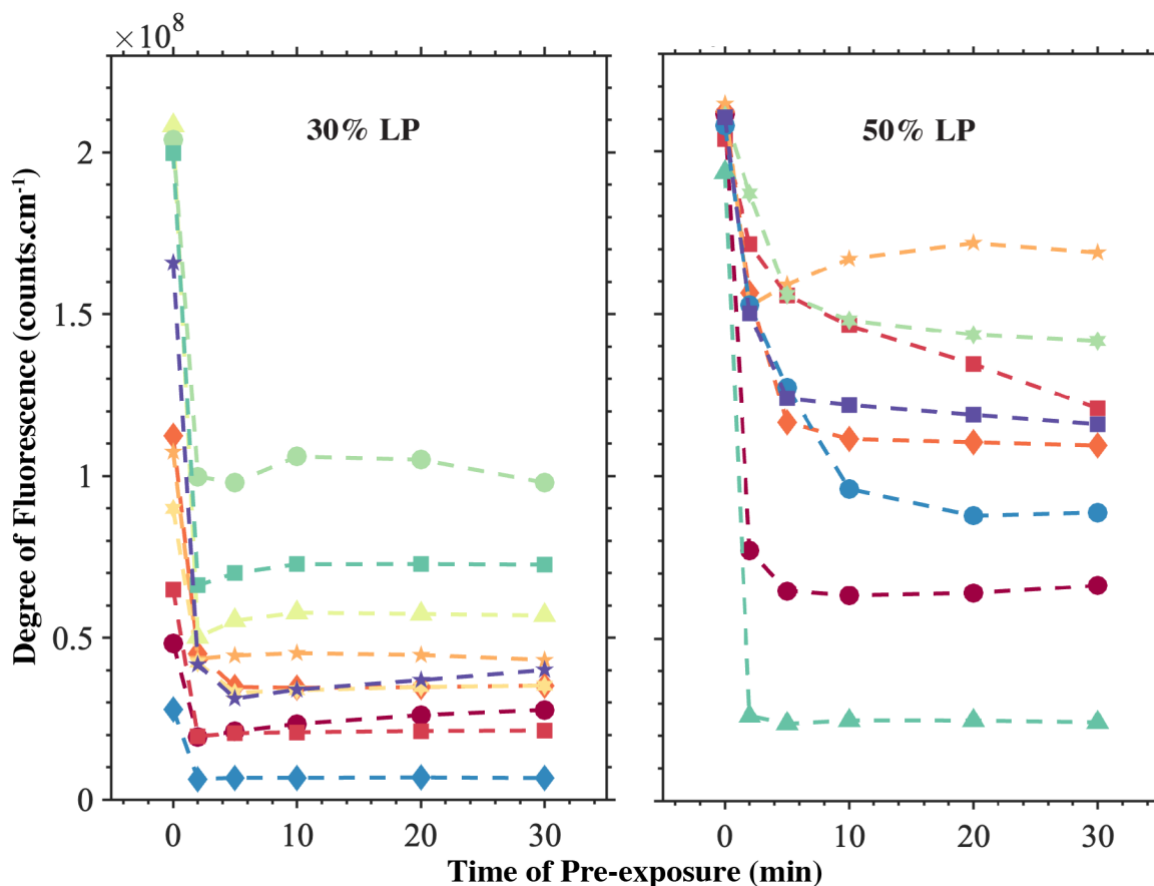
311 locations need not be consistent across different WTE fly ashes, possibly because they depend on
312 thermal maturity for organic matter.^{71,72} For example, the D band position can vary between
313 1257 cm⁻¹ and 1435 cm⁻¹, while the G band position can fluctuate between 1502 cm⁻¹ and 1609 cm⁻¹.
314 The unburnt carbon detected through Raman spectroscopy shows weak Bragg reflections in its
315 powder diffraction pattern.⁷³ Therefore, the existence of carbon is ordinarily not detected through
316 XRD. However, in the case of Raman spectroscopy, the parameters obtained from the peak fitting
317 of G and D bands (peak center and full width at half maximum) can reveal additional structural
318 information about the unburnt carbon, which is critical for carbon-containing WTE fly ashes that
319 may reduce the efficacy of air-entraining agents when upcycled in concrete.^{74,75} In summary, at
320 30% laser power, we detected the presence of calcite, calcium sulfate, zincite, and amorphous
321 carbon in the photobleached spectrum via Raman spectroscopy. WTE fly ashes exhibit similar
322 Raman fluorescence to other industrial waste materials, such as slags.⁷⁶ Hence, photobleaching
323 may reveal additional mineralogical information for such complex systems.

324

325 **Challenges and Limitations in Phase Detection through Raman Spectroscopy**

326 Despite photobleaching, other Raman active phases, such as hydrocalumite, portlandite, quartz,
327 calcium chloride hydroxide, sylvite, and halite detected through power XRD, remained undetected
328 through Raman spectroscopy in these WTE ashes. This apparent absence of phases may be
329 occurring because of several reasons. First, the undetected phases may be present at low
330 concentrations unsuitable for detection via Raman spectroscopy. A way to detect these phases is
331 to increase the laser power. After increasing the laser power to 50 %, we did not identify additional
332 characteristic Raman peaks in the Raman spectrum of WTE fly ashes. As before, the organic
333 species in WTE fly ashes caused a high degree of fluorescence at 50 % laser power. In this context,

334 the degree of fluorescence, calculated as the total spectral count expressed in counts.cm⁻¹, is
335 obtained directly from the raw spectra without subtracting the Raman peaks. This approach is
336 predicated on the assumption that the contribution of Raman peaks to the total counts is negligible
337 compared to the dominant fluorescence and background signals. Notably, during the initial 2
338 minutes of photobleaching, this degree of fluorescence was substantially reduced at 50% laser
339 power (Fig. 3). Photobleaching beyond 2 minutes reduced fluorescence, albeit at a slower rate. We
340 did not attempt to increase the laser power further because the CCD camera systematically reached
341 saturation at higher laser powers. Second, some undetected phases, such as halite and sylvite, have
342 cubic symmetry, and all the atoms forming halite and sylvite are located at inversion centers. Any
343 possible displacement of atoms from the inversion centers would violate symmetry. Therefore,
344 first-order Raman peaks for halite and sylvite are forbidden.⁵⁸ But minerals such as halite and
345 sylvite have weak second-order characteristic Raman peaks. However, these peaks are only seen
346 with large signal accumulation time. In this paper, all the spectra were collected with an
347 accumulation time of 6 seconds, which may have prevented the detection of halite and sylvite.
348 Finally, some phases undetected through Raman spectroscopy may disintegrate when
349 photobleached with laser radiation. This may prevent the detection of phases, such as calcium
350 chloride hydroxide, that disintegrate when exposed to high temperatures (thermogravimetric
351 curves of these phases are presented in Fig. S1). Similar disintegration may also occur with phases
352 that were detected in the Raman spectra of four WTE fly ashes, i.e., calcite, calcium sulfate, and
353 zincite (Fig. 2). Hence, the stability of these phases when photobleached for varying amounts of
354 time must be evaluated. In the next section, we evaluate the stability of calcite, calcium sulfate,
355 zincite, and calcium chloride hydroxide when photobleached.



356
 357 *Fig. 3. The effect of laser power and pre-exposure time on the degree of fluorescence of WTE fly ashes. The*
 358 *degree of fluorescence at 30 and 50 % laser power are calculated from the Raman spectra of WTE fly ashes*
 359 *obtained after 0, 2, 5, 10, 20, and 30 minutes of photobleaching. All the Raman spectra were collected with*
 360 *an acquisition time of 6 seconds. At 30 and 50 % laser power (LP), the CCD detector became saturated for*
 361 *2 and 4 unique WTE fly ash specimens, respectively. As a result, the degree of fluorescence at 30 and 50%*
 362 *LP in Fig. 3 is shown for 10 and 8 unique WTE fly ash specimens, respectively, out of the 12 specimens*
 363 *investigated in this article.*

364

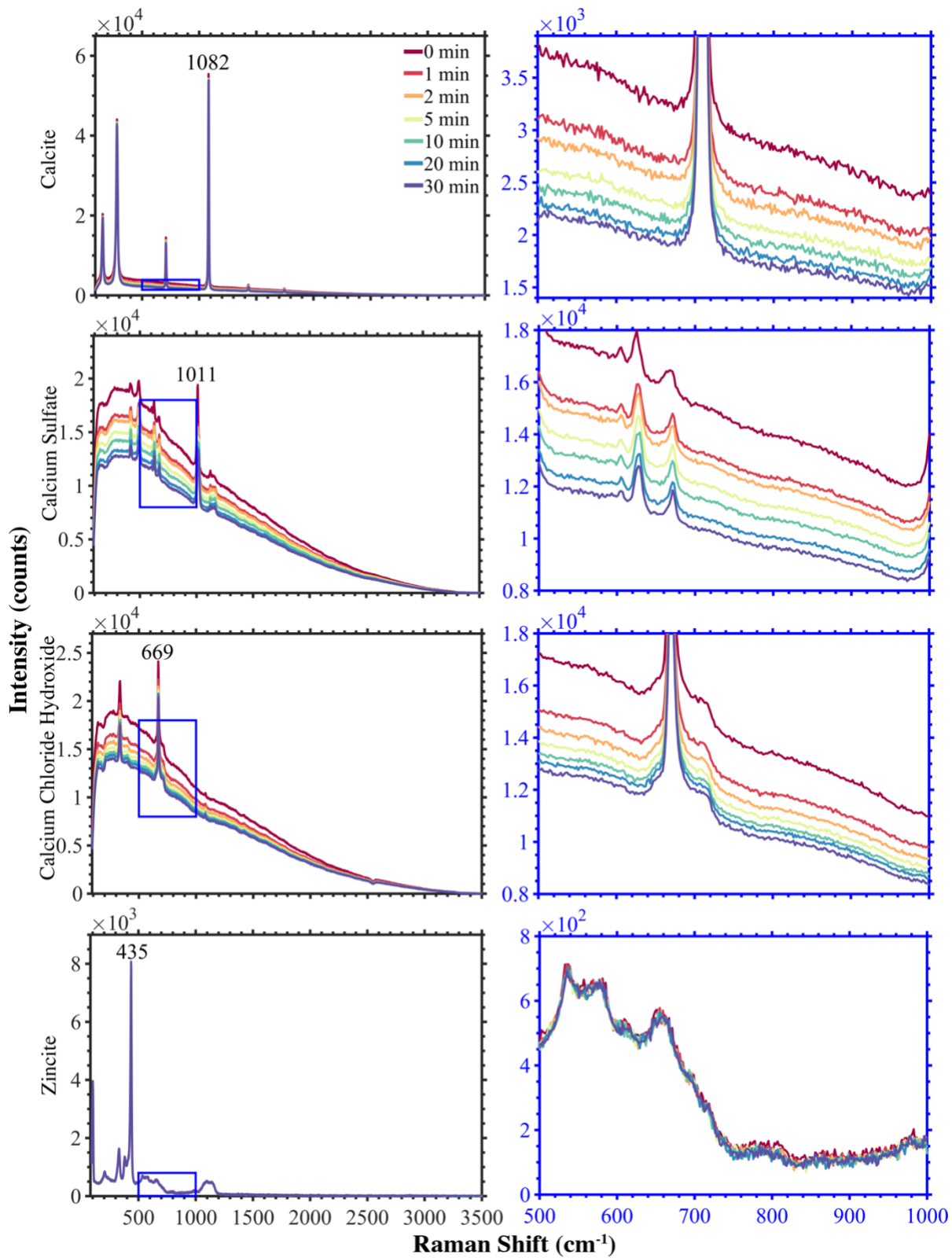
365 3.3. The Effect of Photobleaching on Pure Phases

366 Apart from reducing fluorescence, photobleaching may also result in sample degradation, i.e., the
 367 structural breakdown of phases present in WTE fly ashes.^{63,65} Therefore, it is essential to
 368 understand the effect of photobleaching on minerals commonly found in WTE fly ashes. For this
 369 purpose, we evaluated the effect of photobleaching on commercially available minerals (calcite,
 370 calcium sulfate, and zincite) and calcium chloride hydroxide prepared in the laboratory. The

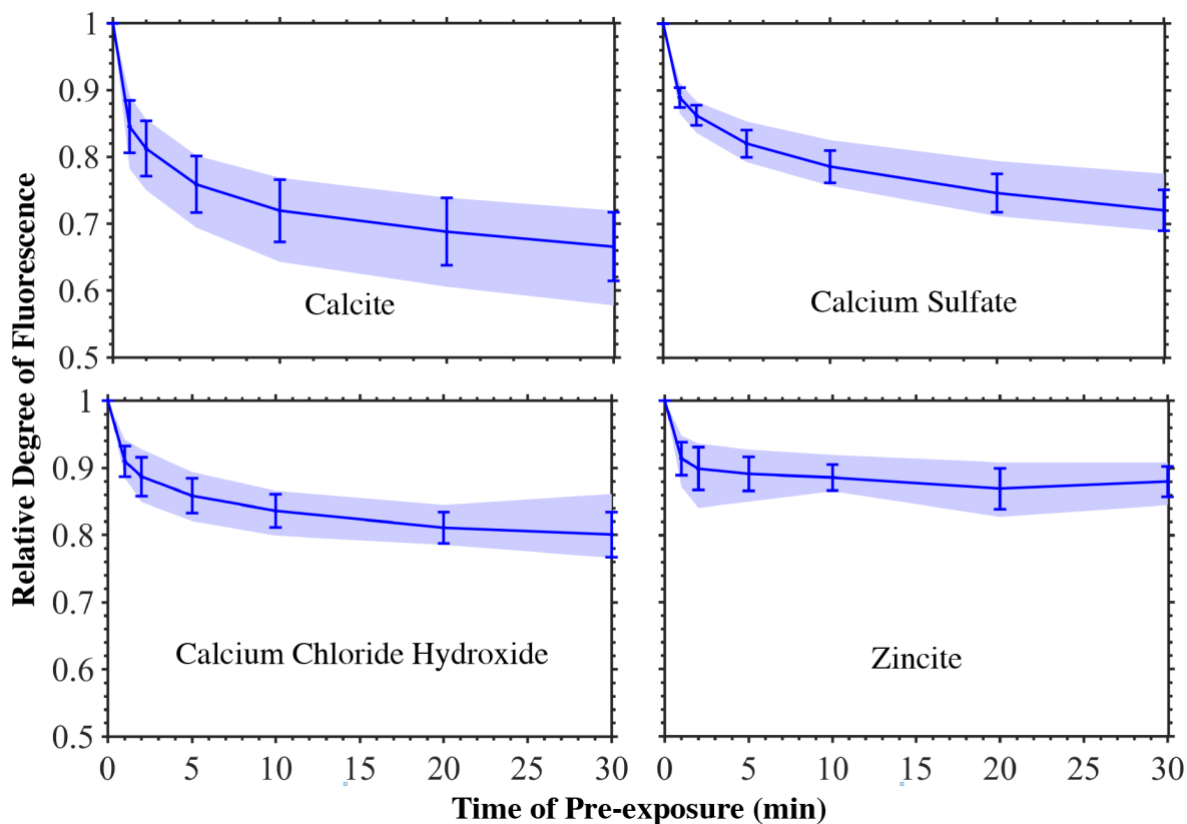
371 powder-XRD patterns for minerals (calcite, calcium sulfate, zincite, and calcium chloride
372 hydroxide) used for evaluating the effect of photobleaching on the Raman spectra are depicted in
373 Fig. S3. Further, the powder-XRD patterns of these minerals were compared with the standard
374 patterns from the International Center for Diffraction Data Powder Diffraction File database (Fig.
375 S3). These comparisons suggest that the calcite, zincite, and calcium chloride hydroxide used in
376 our study were of high purity. In contrast, the used calcium sulfate is a combination of anhydrite,
377 hemihydrate, and gypsum.

378 **Impact of Photobleaching Duration on Raman Spectra of Pure Phases**

379 The Raman spectra of calcite, calcium sulfate, zincite, and calcium chloride hydroxide
380 photobleached for different periods at 90 % laser power are illustrated in Fig. 4. A high laser power
381 of 90 % was selected to evaluate the photobleaching stability. The photobleached Raman spectra
382 of calcite, calcium sulfate, zincite, and calcium chloride hydroxide suggest that these minerals do
383 not disintegrate when photobleached. However, the fluorescence associated with calcite, calcium
384 sulfate, and calcium chloride hydroxide is observed to reduce with photobleaching (Fig. 5). Only
385 marginal reduction is observed in the case of zincite (ZnO), suggesting that photobleaching has no
386 significant impact on the Raman spectra of zincite. Therefore, these results support that 2 minutes
387 is an adequate photobleaching time for WTE ashes comprising these minerals (see section 3.2). In
388 the past, photobleaching has been used to mitigate fluorescence for different systems, including
389 human skin tissue, paints, blood plasma, urine, plant toxins, bone tissue, and textiles.^{62,64,66,67,77–81}
390 The optimal photobleaching time for these systems ranged between seconds and hours. For
391 instance, the Raman spectrum without excessive fluorescence is obtained after 20 seconds of
392 photobleaching for human skin tissue,^{66,79} whereas for plant toxins, a significant reduction in
393 fluorescence was noted after 11 hours of photobleaching.⁷⁷



394
 395 *Fig. 4. The effect of the photobleaching period on the Raman spectra of calcite, calcium sulfate, calcium*
 396 *chloride hydroxide, and zincite. All the Raman spectra were collected with a laser power of 90%*
 397 *(acquisition time = 1 second).*



398
 399 *Fig. 5. The relative degree of fluorescence (normalized to the initial degree of fluorescence) versus pre-*
 400 *exposure time for calcite, calcium sulfate, calcium chloride hydroxide, and zincite(1s acquisition time). The*
 401 *solid medium line represents the average, while the shaded areas represent the maximum and the minimum*
 402 *degree of fluorescence for the different laser powers: 10, 30, 50, 70, and 90%. For each of these pure*
 403 *phases, the effect of laser power and time of pre-exposure on fluorescence is depicted in Fig. S4. The error*
 404 *bars represent the standard error of the mean for relative degree of fluorescence (across different laser*
 405 *powers).*

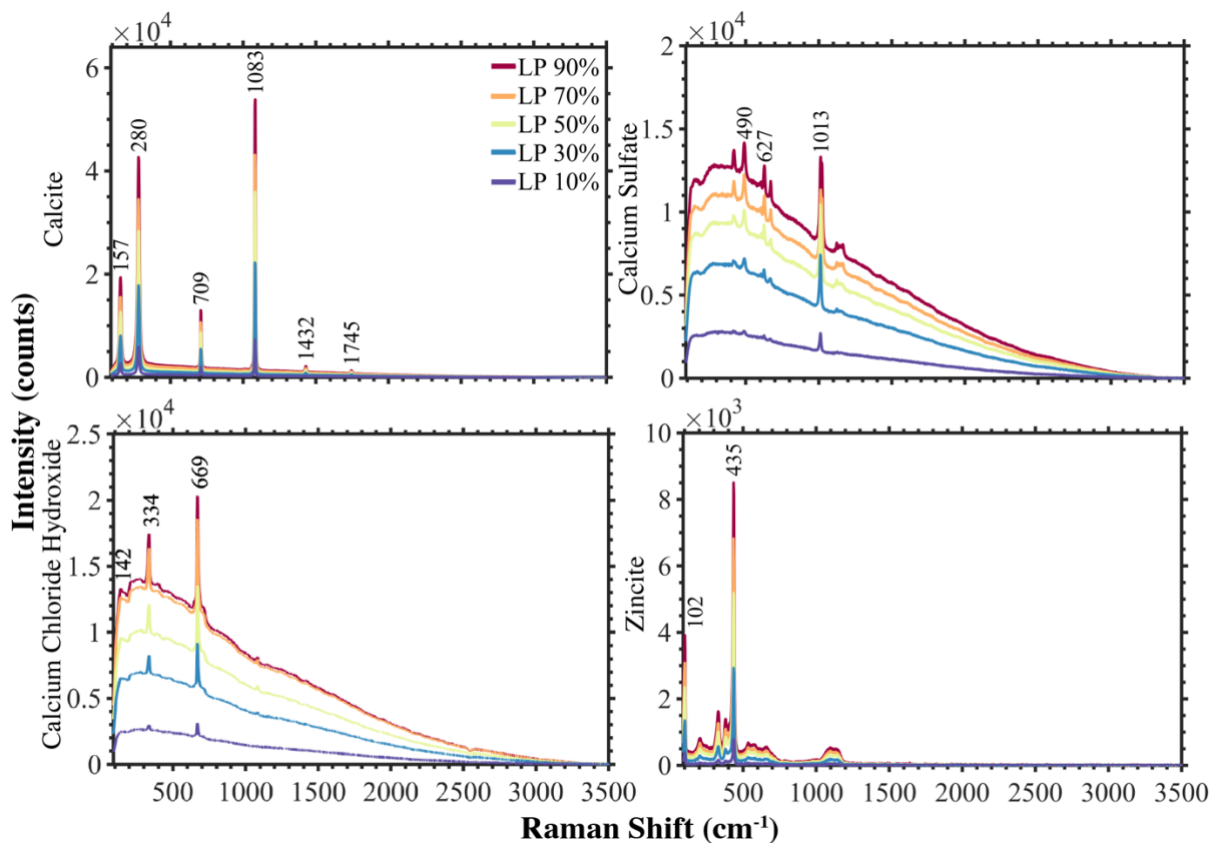
406

407 **Impact of Laser Power on Photobleaching and Raman Peak Intensity for Pure Phases**

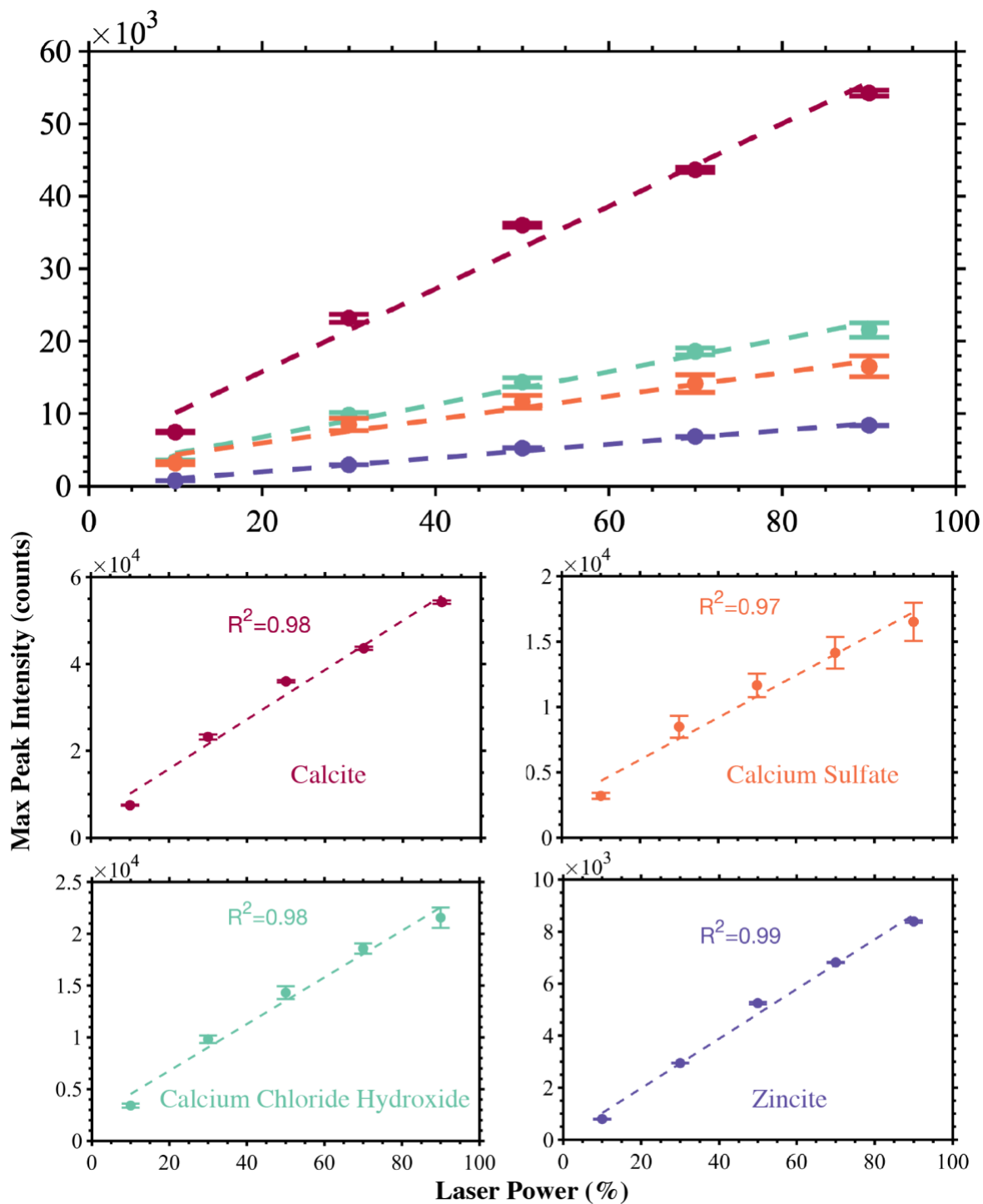
408 The photobleaching duration reduces with an increase in laser power.⁶² Hence, increased laser
 409 power can further reduce the photobleaching duration. However, the laser power can only be
 410 increased to a limited extent because, at higher laser power, the CCD detector may reach saturation.
 411 For instance, on pure phases (calcite, calcium sulfate, calcium chloride hydroxide, and zincite), a
 412 laser power of 90 % did not saturate the CCD detector (Fig. 6). So, Raman spectra could be
 413 collected at high laser power. However, the CCD detector reached saturation when laser power

414 exceeded 50 % for WTE fly ashes (see section 3.2). Therefore, the Raman spectra of WTE fly
415 ashes must be collected at laser powers lower than 50 %. At reduced laser power, the characteristic
416 Raman peak intensity of Raman active phases will likely decrease. We observe a similar decrease
417 in the intensity of characteristic Raman peaks (after 30 minutes of photobleaching) with laser
418 power for pure phases (Fig. 6), i.e., independent of the photobleaching duration, the intensity of
419 characteristic Raman peaks scales linearly with laser power (Fig. 7). In summary, photobleaching
420 reduced the fluorescence in the Raman spectra of pure phases. Additionally, we find that when
421 photobleached, these pure phases (calcite, calcium sulfate, calcium chloride hydroxide, and
422 zincite) are stable and do not disintegrate. These results suggest that Raman spectroscopy coupled
423 with a few minutes of photobleaching does not alter the mineralogy of WTE fly ashes. Earlier, we
424 demonstrated that photobleaching reduced background fluorescence for four selected fly ash
425 specimens (section 3.2). With the evidence that the pure phases are stable under photobleaching,
426 we further evaluated the effect of photobleaching on the Raman spectra of eight additional WTE
427 fly ashes, which are discussed in the next section.

428



429
 430 *Fig. 6. The effect of laser power (LP) on the Raman spectra of calcite, calcium sulfate, calcium chloride*
 431 *hydroxide, and zincite. All the Raman spectra were collected after photobleaching for 30 minutes*
 432 *(acquisition time = 1 second).*



433
 434 Fig. 7. The relationship between the intensity of most prominent Raman characteristic peaks and laser
 435 power (100% corresponds to 450 mW) for calcite, calcium sulfate, calcium chloride hydroxide, and
 436 zincite. Note that the most prominent Raman peaks for calcite, calcium sulfate, calcium chloride hydroxide, and
 437 zincite occur at 1082 cm^{-1} , 1011 cm^{-1} , 669 cm^{-1} , and 435 cm^{-1} . The pure phases were photobleached for
 438 different periods at each laser power. So, for every phase, multiple data points at each laser power
 439 correspond to different photobleaching intervals (0, 1, 2, 5, 10, 20, and 30 minutes). The error bars
 440 represent standard error of the mean for max peak intensity (across different photobleaching intervals).

441

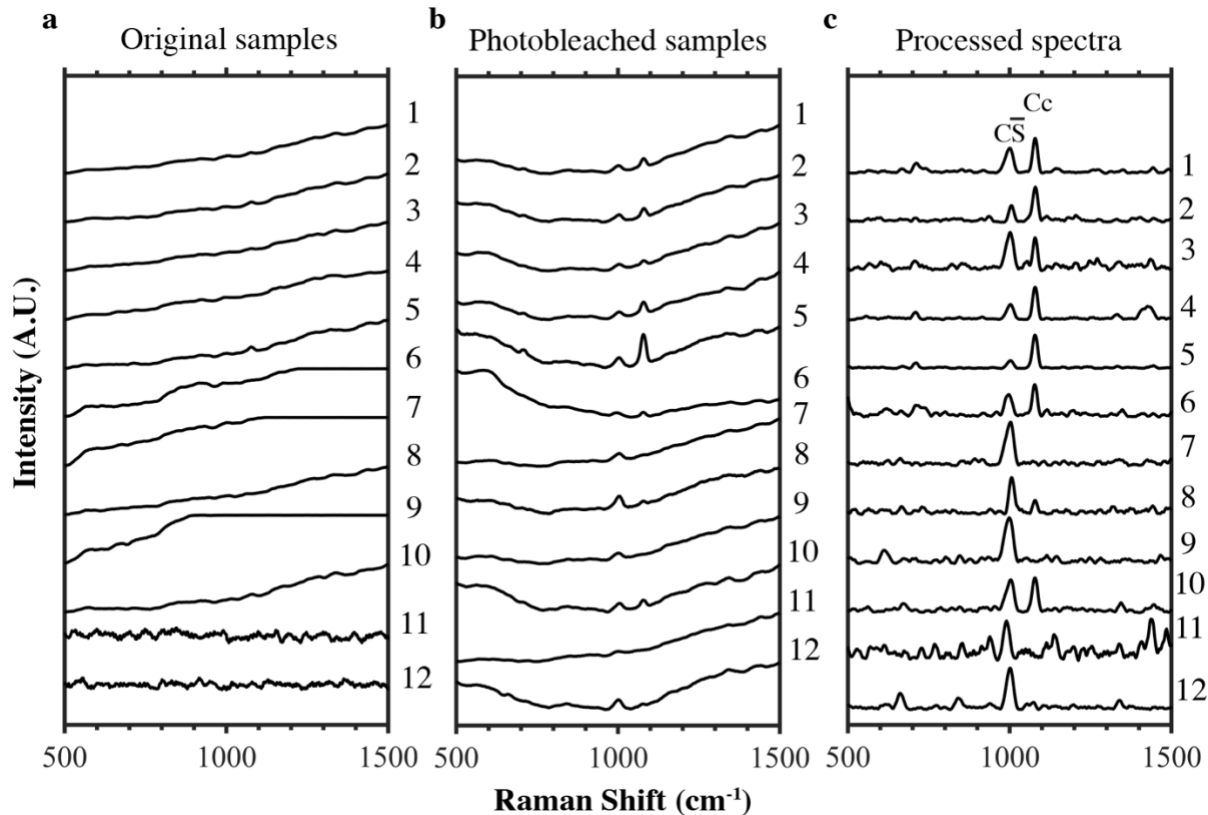
442 **3.4. Photobleaching on Additional WTE Fly Ashes**

443 Our initial investigation into the effect of photobleaching on four selected WTE fly ashes showed
444 a significant reduction in background fluorescence, which enabled the detection of calcite, calcium
445 sulfate, zincite, and carbon in the fly ash specimens without any sample degradation (see section
446 3.2 and 3.3). Here, for further validation, we investigated the effect of photobleaching on eight
447 additional fly ash specimens. The Raman spectra of these eight specimens with the four previous
448 specimens are shown in Fig. 8. As before, for these twelve specimens, we note that without
449 photobleaching, background fluorescence masks the characteristic Raman peaks (Fig. 8a). After
450 photobleaching, the background fluorescence for all twelve specimens reduces considerably,
451 allowing the characteristic Raman peaks to appear (Fig. 8 b).

452

453 Further treatment of the photobleached Raman spectra through a Savitzky-Golay filter (noise
454 suppression), followed by background subtraction and normalization, enables clear identification
455 of characteristic Raman peaks for the most prominent peaks of calcite and calcium sulfate (Fig. 8
456 c). The MATLAB program for processing the photobleached Raman spectra is shared in the
457 supplementary material. After processing, the characteristic Raman peaks at 1083 cm^{-1} and 1013
458 cm^{-1} indicate the presence of calcite and calcium sulfate, respectively. In summary, our
459 investigation on eight additional specimens validates using photobleaching for analyzing WTE fly
460 ashes with Raman spectroscopy. When coupled with photobleaching, we demonstrate that Raman
461 spectroscopy can shed additional information about the mineralogy of WTE fly ash specimens.

462



463
 464 *Fig. 8. Raman spectra of the 12 studied WTE fly ashes: (a) Original Raman spectra without photobleaching.*
 465 *(b) Spectra after 30 min of photobleaching. (c) Spectra after 30 min of photobleaching, noise, and*
 466 *background removal. Cc denotes calcite, CS denotes calcium sulfate. All the Raman spectra in this figure*
 467 *were collected with an acquisition time of 6 seconds, and the laser power is fixed at 30 % (135 mW).*
 468

469 **3.5. Photobleaching Mechanisms in WTE Fly Ashes**

470 In this article, we demonstrated that photobleaching can reduce fluorescence in the Raman spectra
 471 of WTE fly ash specimens, enabling the identification of mineralogical species. We consider that
 472 the observed decrease in fluorescence results from three possible mechanisms. The first
 473 mechanism is based on previous investigations that studied the commonly occurring
 474 photobleaching phenomenon in fluorescence microscopy-based techniques, such as confocal laser-
 475 scanning microscopy.^{83,84} In fluorescence microscopy-based techniques, specimens with
 476 fluorescent probes (for example, dyes or stable fluorophores) are irradiated with a laser, and the
 477 resulting fluorescence signal is used for imaging biological (organic) specimens. The exposure of

478 the fluorophore to a laser source can reduce or permanently extinguish its ability to fluoresce.⁸²⁻⁸⁷
479 This reduction in fluorescence is caused by the fluorophore molecules excited to high-energy states
480 by laser exposure. For example, as a result of laser exposure, fluorophore molecules can be excited
481 from ground energy level (S) to singlet-excited energy level (S*) and excited triplet state (T*⁶⁰.
482 Excited fluorophore molecules can react with molecular oxygen, if present, and generate reactive
483 oxygen species (peroxides, hydroxyl radicals, superoxide anion, and singlet oxygen) that can
484 oxidize organic fluorophores and eliminate its capability to fluoresce. In the absence of molecular
485 oxygen, fluorophores in excited states have increased reactivity in electron transfer reactions,
486 which leads to the formation of non-fluorescent radical species, extinguishing their capability to
487 fluoresce permanently.^{60,88} Organic species occur in WTE fly ashes, which may have the capability
488 to fluoresce. As discussed, these organic species may be able to fluoresce like fluorophores on
489 laser exposure, resulting in the photobleaching observed in our experiments.

490
491 The second pathway that can cause the observed photobleaching is photochemical processes, such
492 as photoionization and bond fission.⁸⁸ Excited fluorophore molecules (excited because of laser
493 exposure) will relax from high-energy states and release energy, which may cause localized
494 heating. The released heat may not dissipate rapidly and accumulate, possibly resulting in the
495 thermal destruction of species responsible for causing fluorescence in the Raman spectrum of WTE
496 fly ashes. Finally, the third suggested mechanism is based on the observation that the fluorescence
497 in the Raman spectrum of inorganic mineralogical species (pure phases) decreases after
498 photobleaching (see section 3.3). Unlike organic fluorophores, inorganic materials are much more
499 photostable – they likely do not react with reactive oxygen species, form radical species, and
500 undergo thermal destruction. Therefore, the observed photobleaching in inorganic materials must

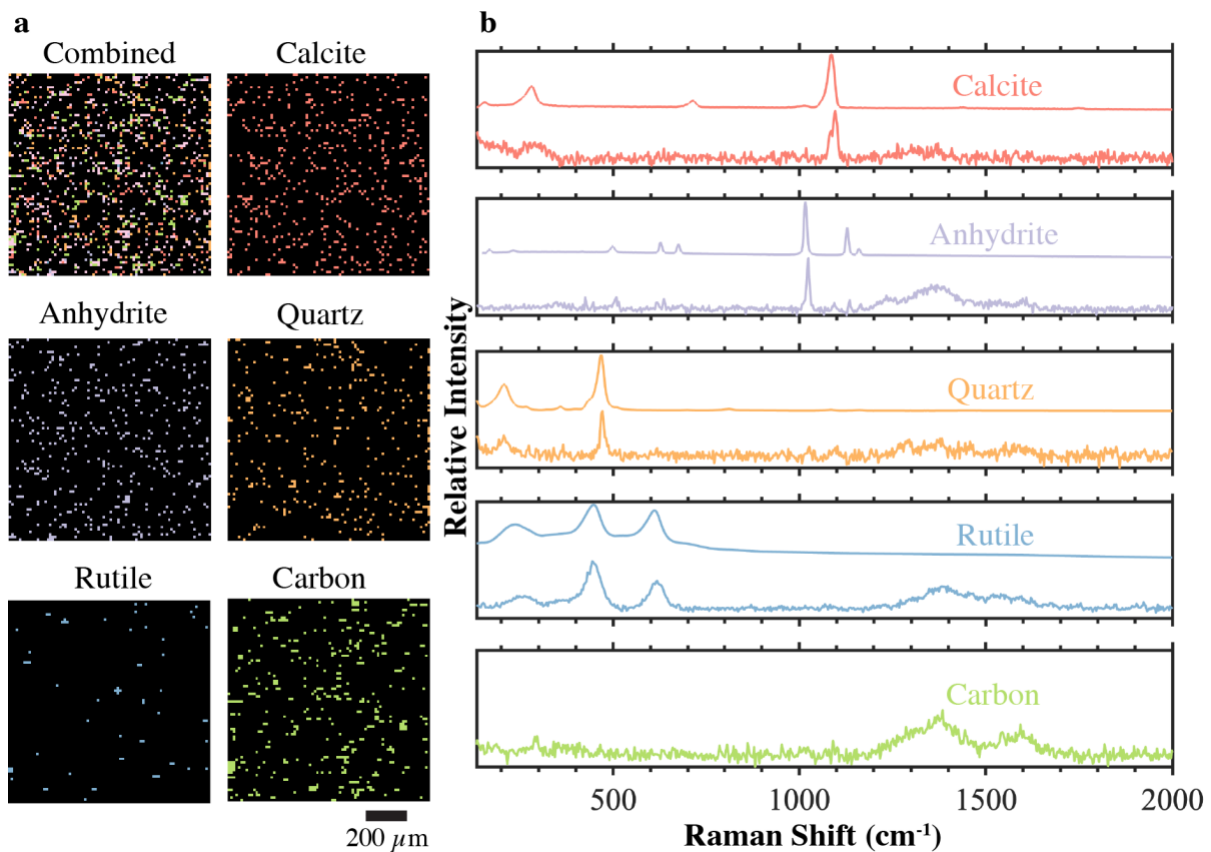
501 occur via an alternative pathway. We suggest that due to localized heating, inorganic materials
502 (pure phases) undergo expansion, reducing the porosity of the area interacting with the laser
503 source. The reduction in porosity means that the area occupied by air voids in the pellet specimen
504 in contact with the laser diminishes, resulting in a reduced extent of mismatch between the
505 refractive index at the void and ash particle interface. As a result of a decreased extent of mismatch
506 in the refractive index at the interface, there is reduced scattering of the incident laser, resulting in
507 the reduced background (fluorescence) in the Raman spectrum of inorganic materials.⁶⁶ A
508 schematic depicting the third mechanism is shown in the supplementary information (Fig. S6).
509 Since WTE fly ashes are comprised of organic and inorganic species, all three mechanisms may
510 be responsible for the photobleaching phenomenon.

511

512 **3.6. Complementarity of Raman Spectroscopy to X-ray Diffraction and X-ray** 513 **Fluorescence**

514 A detailed understanding of WTE ash composition (elemental and mineralogical) is essential for
515 finding composition-compatible end uses for ash upcycling. The most widely used analytical
516 technique for determining the elemental composition of WTE ashes is X-ray fluorescence (XRF).
517 In XRF, an analytical sample is irradiated with X-rays, which generates fluorescent X-rays in the
518 sample.³⁵ These fluorescent X-rays are measured and subsequently used for quantifying the
519 elemental concentration. The elemental concentration obtained from XRF is often expressed in
520 terms of the weight percentages of the oxides of the elements present in a sample.⁸⁹ This practice
521 of expressing elemental concentrations as equivalent oxide concentrations is made under the
522 assumption that the elements in a given sample are directly bonded to oxygen. However, such
523 assumptions are not necessarily accurate. For example, Zn in WTE fly ashes can exist in multiple

524 speciations, such as $Zn_4Si_2O_7(OH)_2 \cdot H_2O$, $ZnFe_2O_4$, $ZnAl_2O_4$, ZnO , $Zn(OH)_2$, $Zn_5(CO_3)_2(OH)_6$,
 525 and $ZnCl_2$.³⁴ Therefore, alternative characterization methods for understanding elemental
 526 speciation are necessary. Typically, the speciation of different elements in WTE fly ashes is
 527 determined through powder X-ray diffraction. However, this technique has two limitations. First,
 528 it cannot characterize WTE fly ashes in real-time. Second, the speciation of minor elements, i.e.,
 529 Zn, Ti, Br, and Pb (< 5 weight % concentration, Fig. 1b), is not often resolved with powder X-ray
 530 diffraction due to significant overlaps in the powder X-ray diffraction pattern of WTE fly ashes.



531
 532 *Fig. 9. Raman hyperspectral phase maps of mineralogical species present in WTE fly ash 12: (a) Combined*
 533 *and individual phase maps. (b) Experimental and reference Raman spectra of mineralogical species*
 534 *identified in WTE fly ash 12 specimen. Note that the experimental Raman spectra (bottom spectrum in each*
 535 *subplot) were obtained after true component analysis, whereas the depicted reference Raman spectra (top*
 536 *spectrum in each subplot) are from the RRUFF database. The RRUFF reference id for calcite, anhydrite,*
 537 *quartz, and rutile shown in Fig. 9b are R040170, R040061, R040031, and R060493. In the combined map,*
 538 *pink pixels have multiple phases.*
 539

540 These two limitations of powder X-ray diffraction can be overcome to some extent with Raman
541 spectroscopy. We observed in our study that a mere two minutes of photobleaching allows a
542 significant reduction in fluorescence, enabling the identification of elemental speciation in real-
543 time (see section 3.2). Additionally, we resolved the speciation of minor elements such as Zn with
544 Raman spectroscopy. In Raman spectroscopy, the characteristic Raman peaks represent molecular
545 vibrational characteristics (changes in polarizability) – a distinct attribute for each mineral species
546 in WTE fly ashes.³⁶ Some mineral species in low concentration are not identifiable with powder
547 X-ray diffraction. However, these low-concentration mineral species may have strong Raman
548 scattering capability, which may enable their identification with Raman spectroscopy. An example
549 of this is Zincite (ZnO) – a mineral phase that we could not detect with powder X-ray diffraction,
550 but Raman spectroscopy suggested its presence (see section 3.2, Fig. 2). On the contrary, some
551 mineral species are not Raman active or their Raman scattering capability is inherently weak (at a
552 given concentration). Hence, they are not detected through Raman spectroscopy. For example, we
553 could detect the presence of hydrocalumite, portlandite, quartz, calcium chloride hydroxide,
554 sylvite, and halite through X-ray diffraction (see section 3.1). However, these phases could not be
555 detected through Raman spectroscopy (see section 3.2).

556

557 Some of the limitations of Raman spectroscopy can be overcome with Raman hyperspectral
558 imaging. With Raman hyperspectral imaging, samples can be probed at a sub-micrometer
559 resolution.⁹⁰ At sub-micrometer resolution, mineralogical species undetected through Raman
560 spectroscopy due to their low concentrations (with respect to the bulk) can be identified because
561 these species are typically heterogeneously distributed within a sample and are locally abundant
562 on a given spot at the sub-micrometer scale. In this study, we selected one WTE fly ash specimen

563 and investigated its mineralogy through Raman hyperspectral imaging with a spot size of 0.95 μm .
564 With Raman hyperspectral imaging, we were able to identify the presence of calcite, anhydrite,
565 quartz, rutile, and carbon in WTE fly ash 12 (Fig. 9). These results from Raman hyperspectral
566 imaging agree with our findings with Raman spectroscopy (see section 3.2), wherein we observed
567 the presence of calcite, anhydrite, and carbon. Additionally, we note that with Raman hyperspectral
568 imaging, we identified phases like quartz and rutile, the latter being confirmed with its broad peaks
569 at 447 and 611 cm^{-1} (Fig. 9). Although these peaks were present in the initial Raman spectroscopy
570 (Fig. 2), their subtle and broad nature did not draw our attention. However, a retrospective
571 examination of (Fig. 2), post-photobleaching, made these peaks more discernible, revealing the
572 presence of rutile and confirming our findings through Raman hyperspectral imaging. However,
573 we emphasize that Raman hyperspectral imaging of a single ash specimen (1 mm \times 1 mm area)
574 took approximately 2 hours, whereas phase identification with Raman spectroscopy merely took
575 2 minutes. Despite being time intensive, Raman hyperspectral imaging can also help uncover the
576 mineralogy of toxic elements (Pb and Cd) in WTE fly ashes. For example, Pb and Cd in WTE fly
577 ashes are reported to exist in the form of Raman active mineral species, such as CdSO_4 , CdO , PbO ,
578 PbCl_2 , and PbS .⁹¹⁻⁹⁶ In summary, Raman spectroscopy can provide mineral phase information
579 complementary to X-ray diffraction and X-ray fluorescence in real-time.

580

581 **4. Conclusions**

582 The chemical characteristics of waste-to-energy (WTE) ashes depend on several factors, including
583 the input waste composition and the incineration conditions at the WTE facility. These factors can
584 vary widely; as a result, the chemical characteristics of WTE fly ashes can show significant
585 variation. The variability in composition makes WTE fly ashes unsuitable for any single upcycling

586 application. Therefore, there is a need for a method that can rapidly characterize the mineralogy
587 of these ashes. In this study, we evaluated the possibility of employing Raman spectroscopy to
588 elucidate the mineralogical characteristics of WTE fly ashes. Our results indicated that the WTE
589 fly ashes show excessive fluorescence when probed through typical Raman spectroscopy,
590 obscuring any meaningful interpretation of the Raman spectra. To resolve this issue, we reported
591 that the excessive fluorescence arising in WTE fly ashes could be overcome by a few minutes of
592 photobleaching, i.e., by exposing ash specimens to laser radiation before data collection. The
593 photobleached Raman spectra suggested the presence of calcite, calcium sulfate, zincite, and
594 amorphous carbon (graphitic and disordered bands) in WTE fly ashes. Most importantly, the
595 fluorescence in the Raman spectrum of WTE fly ashes was reduced to an acceptable degree after
596 mere 2 minutes of photobleaching, suggesting that Raman spectroscopy can be a useful method to
597 monitor the mineralogical characteristics of WTE fly ashes in a rapid fashion. Finally, we
598 evaluated the photobleaching stability for four key phases – calcite, calcium sulfate, zincite, and
599 calcium chloride hydroxide. Our investigations demonstrated that these phases are stable against
600 photobleaching, and the fluorescence in the Raman spectra of these phases reduces when
601 photobleached for ~5 minutes. These results signify the utility of Raman spectroscopy in
602 monitoring the mineralogical characteristics of WTE fly ashes rapidly and reliably. In the future,
603 the ability to characterize ashes (e.g., in real-time at a WTE facility) could help divert them from
604 landfills to composition-dependent upcycling pathways.

605

606

607 **Acknowledgments**

608

609 The information, data, or work presented herein was funded by the Advanced Research Projects

610 Agency-Energy (ARPA-E), U.S. Department of Energy, under Award Number DE-AR0001401.

611 The views and opinions of authors expressed herein do not necessarily state or reflect those of the

612 United States Government or any agency thereof. The authors would like to acknowledge that a

613 part of this research was carried out at the Materials Research Laboratory Central Research

614 Facilities and Core Facilities at the Carl R. Woese Institute of Genomic Biology at the University

615 of Illinois Urbana-Champaign. We thank Chirayu Kothari for his MATLAB code, enabling pixel

616 assignment to different phases based on the signal-to-noise (S/N) ratio.

617

618 **References**

619

- 620 1. Kaza S, Yao L, Bhada-Tata P & Van Woerden F. *What a waste 2.0: A global snapshot of*
621 *solid waste management to 2050*. (World Bank, 2018).
- 622 2. Chen, D. M. C., Bodirsky, B. L., Krueger, T., Mishra, A. & Popp, A. The world’s growing
623 municipal solid waste: trends and impacts. *Environmental Research Letters* **15**, (2020).
- 624 3. Gómez-Sanabria, A., Kiesewetter, G., Klimont, Z., Schoepp, W. & Haberl, H. Potential for
625 future reductions of global GHG and air pollutants from circular waste management
626 systems. *Nat Commun* **13**, 1–12 (2022).
- 627 4. Kalogirou, E. N. *Waste-to-energy technologies and global applications*. (CRC Press, 2017).
628 doi:10.1201/9781315269061.
- 629 5. Kumar, V. & Garg, N. National and regional waste stream in the United States:
630 conformance and disparity. *Environmental Research: Infrastructure and Sustainability* **1**,
631 1–12 (2021).
- 632 6. Šyc, M. *et al.* Metal recovery from incineration bottom ash: State-of-the-art and recent
633 developments. *J Hazard Mater* **393**, (2020).
- 634 7. Bertolini, L., Carsana, M., Cassago, D., Curzio, A. Q. & Collepardi, M. MSWI ashes as
635 mineral additions in concrete. *Cem Concr Res* **34**, 1899–1906 (2004).
- 636 8. Qiao, X. C., Tyrer, M., Poon, C. S. & Cheeseman, C. R. Novel cementitious materials
637 produced from incinerator bottom ash. *Resour Conserv Recycl* **52**, 496–510 (2008).
- 638 9. Ginés, O., Chimenos, J. M., Vizcarro, A., Formosa, J. & Rosell, J. R. Combined use of
639 MSWI bottom ash and fly ash as aggregate in concrete formulation: Environmental and
640 mechanical considerations. *J Hazard Mater* **169**, 643–650 (2009).
- 641 10. Mathews, G., Sinnan, R. & Young, M. Evaluation of reclaimed municipal solid waste
642 incinerator sands in concrete. *J Clean Prod* **229**, 838–849 (2019).
- 643 11. Sarmiento, L. M., Clavier, K. A., Paris, J. M., Ferraro, C. C. & Townsend, T. G. Critical
644 examination of recycled municipal solid waste incineration ash as a mineral source for
645 portland cement manufacture – A case study. *Resour Conserv Recycl* **148**, 1–10 (2019).
- 646 12. Clavier, K. A. *et al.* Washed waste incineration bottom ash as a raw ingredient in cement
647 production: Implications for lab-scale clinker behavior. *Resour Conserv Recycl* **169**, (2021).
- 648 13. Poly, F., Gros, R., Jocteur-Monrozier, L. & Perrodin, Y. Short-term changes in bacterial
649 community fingerprints and potential activities in an alfisol supplemented with solid waste
650 leachates. *Environ Sci Technol* **36**, 4729–4734 (2002).
- 651 14. Falcoz, Q., Gauthier, D., Abanades, S., Flamant, G. & Patisson, F. Kinetic rate laws of Cd,
652 Pb, and Zn vaporization during municipal solid waste incineration. *Environ Sci Technol* **43**,
653 2184–2189 (2009).
- 654 15. Aubert, J. E., Mahieux, P. Y. & Husson, B. Mineralogical transformations during a
655 stabilization process developed for the valorization of municipal solid waste incineration
656 (MSWI) fly ash. *Waste Biomass Valorization* **1**, 261–270 (2010).
- 657 16. Bui Viet, D. *et al.* The use of fly ashes from waste-to-energy processes as mineral CO2
658 sequestrers and supplementary cementitious materials. *J Hazard Mater* **398**, 122906 (2020).
- 659 17. Ren, P., Ling, T. C. & Mo, K. H. CO2 pretreatment of municipal solid waste incineration
660 fly ash and its feasible use as supplementary cementitious material. *J Hazard Mater* **424**,
661 127457 (2022).
- 662 18. Kumar, V. & Garg, N. The chemical and physical origin of incineration ash reactivity in
663 cementitious systems. *Resour Conserv Recycl* **177**, (2022).

- 664 19. Garg, N. & White, C. E. Mechanism of zinc oxide retardation in alkali-activated materials:
665 an in situ X-ray pair distribution function investigation. *J Mater Chem A Mater* **5**, 11794–
666 11804 (2017).
- 667 20. Kumar, V. & Garg, N. The chemical and physical origin of incineration ash reactivity in
668 cementitious systems. *Resour Conserv Recycl* **177**, 106009 (2022).
- 669 21. Alba, N., Gassó, S., Lacorte, T. & Baldasano, J. M. Characterization of municipal solid
670 waste incineration residues from facilities with different air pollution control systems. *J Air*
671 *Waste Manage Assoc* **47**, 1170–1179 (1997).
- 672 22. Haberl, J., Koralewska, R., Schlumberger, S. & Schuster, M. Quantification of main and
673 trace metal components in the fly ash of waste-to-energy plants located in Germany and
674 Switzerland: An overview and comparison of concentration fluctuations within and between
675 several plants with particular focus on valuable metals. *Waste Management* **75**, 361–371
676 (2018).
- 677 23. Nedkvitne, E. N., Borgan, Ø., Eriksen, D. Ø. & Rui, H. Variation in chemical composition
678 of MSWI fly ash and dry scrubber residues. *Waste Management* **126**, 623–631 (2021).
- 679 24. Belevi, H. & Moench, H. Factors determining the element behavior in municipal solid waste
680 incinerators. 1. Field studies. *Environ Sci Technol* **34**, 2501–2506 (2000).
- 681 25. Belevi, H. & Langmeier, M. Factors determining the element behavior in municipal solid
682 waste incinerators. 2. Laboratory experiments. *Environ Sci Technol* **34**, 2507–2512 (2000).
- 683 26. Zhou, H., Long, Y., Meng, A., Li, Q. & Zhang, Y. Classification of municipal solid waste
684 components for thermal conversion in waste-to-energy research. *Fuel* **145**, 151–157 (2015).
- 685 27. Bausach, M., Krammer, G. & Cunill, F. Reaction of Ca(OH)₂ with HCl in the presence of
686 water vapour at low temperatures. *Thermochim Acta* **421**, 217–223 (2004).
- 687 28. Partanen, J., Backman, P., Backman, R. & Hupa, M. Absorption of HCl by limestone in hot
688 flue gases. Part I: The effects of temperature, gas atmosphere and absorbent quality. *Fuel*
689 **84**, 1664–1673 (2005).
- 690 29. Partanen, J., Backman, P., Backman, R. & Hupa, M. Absorption of HCl by limestone in hot
691 flue gases. Part II: Importance of calcium hydroxychloride. *Fuel* **84**, 1674–1684 (2005).
- 692 30. Hsiao, M. C., Wang, H. P. & Yang, Y. W. EXAFS and XANES studies of copper in a
693 solidified fly ash. *Environ Sci Technol* **35**, 2532–2535 (2001).
- 694 31. Hsiao, M. C., Wang, H. P., Huang, Y.-J. & Yang, Y. W. EXAFS study of copper in waste
695 incineration fly ashes. *J. Synchrotron Rad* vol. 8 (2001).
- 696 32. Hsiao, M. C., Wang, H. P., Wei, Y. L., Chang, J.-E. & Jou, C. J. Speciation of copper in the
697 incineration fly ash of a municipal solid waste. *J Hazard Mater* **91**, 301–307 (2002).
- 698 33. Hsiao, M. C., Wang, H. P., Chang, J. E. & Peng, C. Y. Tracking of copper species in
699 incineration fly ashes. *J Hazard Mater* **138**, 539–542 (2006).
- 700 34. Rissler, J., Klementiev, K., Dahl, J., Steenari, B. M. & Edo, M. Identification and
701 quantification of chemical forms of Cu and Zn in MSWI ashes using XANES. *Energy and*
702 *Fuels* **34**, 14505–14514 (2020).
- 703 35. Beckhoff, B., Birgit Kanngießer, Norbert Langhoff, Reiner Wedell & Helmut Wolff.
704 *Handbook of practical X-ray fluorescence analysis*. (Springer, 2006).
- 705 36. Srivastava, S. & Garg, N. Tracking spatiotemporal evolution of cementitious carbonation
706 via Raman imaging. *Journal of Raman Spectroscopy* (2022) doi:10.1002/jrs.6483.
- 707 37. Polavaram, K. C. & Garg, N. Enabling phase quantification of anhydrous cements via
708 Raman imaging. *Cem Concr Res* **150**, (2021).

- 709 38. Loh, H. C., Kim, H. J., Ulm, F. J. & Masic, A. Time-space-resolved chemical deconvolution
710 of cementitious colloidal systems using Raman spectroscopy. *Langmuir* **37**, 7019–7031
711 (2021).
- 712 39. Ge, K., Hu, Y. & Li, G. Fabrication of branched gold copper nanoalloy doped mesoporous
713 graphitic carbon nitride hybrid membrane for surface-enhanced Raman spectroscopy
714 analysis of carcinogens. *J Hazard Mater* **432**, (2022).
- 715 40. Luo, Y., Awoyemi, O. S., Naidu, R. & Fang, C. Detection of microplastics and nanoplastics
716 released from a kitchen blender using Raman imaging. *J Hazard Mater* **453**, (2023).
- 717 41. Polavaram, K. C. & Garg, N. Elucidating the size and shape of individual clinker phases via
718 Raman imaging: Impact on cement hydration. *The Journal of Physical Chemistry C* (2023)
719 doi:10.1021/acs.jpcc.3c03453.
- 720 42. Zhang, Z. M. *et al.* An intelligent background-correction algorithm for highly fluorescent
721 samples in Raman spectroscopy. *Journal of Raman Spectroscopy* **41**, 659–669 (2010).
- 722 43. Lutz, H. D., Schmidt, M. & Weckler, B. Infrared and Raman studies on calcium, zinc and
723 cadmium hydroxide halides $\text{Ca}\{\text{O}(\text{H,D})\}\text{Cl}$, $\text{Cd}\{\text{O}(\text{H,D})\}\text{Cl}$, $\text{Zn}\{\text{O}(\text{H,D})\}\text{F}$ and β -
724 $\text{Zn}\{\text{O}(\text{H,D})\}\text{Cl}$. *Journal of Raman Spectroscopy* **24**, 797–804 (1993).
- 725 44. Weckler, B. & Lutz, H. D. Near-infrared spectra of $\text{M}(\text{OH})\text{Cl}$ ($\text{M} = \text{Ca}, \text{Cd}, \text{Sr}$), $\text{Zn}(\text{OH})\text{F}$,
726 γ - $\text{Cd}(\text{OH})_2$, $\text{Sr}(\text{OH})_2$, and brucite-type hydroxides $\text{M}(\text{OH})_2$ ($\text{M} = \text{Mg}, \text{Ca}, \text{Mn}, \text{Fe}, \text{Co}, \text{Ni},$
727 Cd). *Spectrochim Acta A Mol Biomol Spectrosc* **52**, 1507–1513 (1996).
- 728 45. Gilfrich, J. *Handbook of X-Ray Spectrometry*. *X-Ray Spectrometry* vol. 23 (CRC Press,
729 2001).
- 730 46. Wang, H., Mann, C. K. & Vickers, T. J. Effect of powder properties on the intensity of
731 Raman scattering by crystalline solids. *Appl Spectrosc* **56**, 1538–1544 (2002).
- 732 47. Jin, J. W. *et al.* Quantitative spectroscopic analysis of heterogeneous mixtures: The
733 correction of multiplicative effects caused by variations in physical properties of samples.
734 *Anal Chem* **84**, 320–326 (2012).
- 735 48. Chen, Z. P. *et al.* Quantitative analysis of powder mixtures by raman spectrometry: The
736 influence of particle size and its correction. *Anal Chem* **84**, 4088–4094 (2012).
- 737 49. Gómez, D. A., Coello, J. & MasPOCH, S. The influence of particle size on the intensity and
738 reproducibility of Raman spectra of compacted samples. *Vib Spectrosc* **100**, 48–56 (2019).
- 739 50. Zhang, K., Yio, M. H. N., Wong, H. S. & Buenfeld, N. R. Optimising confocal Raman
740 microscopy for spectral mapping of cement-based materials. *Materials and*
741 *Structures/Materiaux et Constructions* **55**, (2022).
- 742 51. Song, G. J., Kim, K. H., Seo, Y. C. & Kim, S. C. Characteristics of ashes from different
743 locations at the MSW incinerator equipped with various air pollution control devices. *Waste*
744 *Management* **24**, 99–106 (2004).
- 745 52. Ma, W., Hoffmann, G., Schirmer, M., Chen, G. & Rotter, V. S. Chlorine characterization
746 and thermal behavior in MSW and RDF. *J Hazard Mater* **178**, 489–498 (2010).
- 747 53. Liu, J., Hu, L., Tang, L. & Ren, J. Utilisation of municipal solid waste incinerator (MSWI)
748 fly ash with metakaolin for preparation of alkali-activated cementitious material. *J Hazard*
749 *Mater* **402**, (2021).
- 750 54. Wang, L., Jin, Y. & Nie, Y. Investigation of accelerated and natural carbonation of MSWI
751 fly ash with a high content of Ca. *J Hazard Mater* **174**, 334–343 (2010).
- 752 55. Frost, R. L., Palmer, S. J. & Theiss, F. Synthesis and Raman spectroscopic characterisation
753 of hydrotalcites based on the formula $\text{Ca}_6\text{Al}_2(\text{CO}_3)(\text{OH})_{16} \cdot 4\text{H}_2\text{O}$. *Journal of Raman*
754 *Spectroscopy* **42**, 1163–1167 (2011).

- 755 56. Schmida, T. & Dariz, P. Shedding light onto the spectra of lime: Raman and luminescence
756 bands of CaO, Ca(OH)₂ and CaCO₃. *Journal of Raman Spectroscopy* **46**, 141–146 (2014).
- 757 57. Ciobotă, V. *et al.* Identification of minerals and organic materials in Middle Eocene
758 ironstones from the Bahariya Depression in the Western Desert of Egypt by means of micro-
759 Raman spectroscopy. *Journal of Raman Spectroscopy* **43**, 405–410 (2012).
- 760 58. Chukanov, N. & Viggasina, M. *Vibrational (infrared and Raman) spectra of minerals and
761 related compounds*. (Springer Mineralogy, 2020).
- 762 59. Edwards, H. G. M., Villar, S. E. J., Jehlicka, J. & Munshi, T. FT-Raman spectroscopic study
763 of calcium-rich and magnesium-rich carbonate minerals. in *Spectrochimica Acta - Part A:
764 Molecular and Biomolecular Spectroscopy* vol. 61 2273–2280 (2005).
- 765 60. Andò, S. & Garzanti, E. Raman spectroscopy in heavy-mineral studies. *Geol Soc Spec Publ*
766 **386**, 395–412 (2014).
- 767 61. Pelletier, M. J. & Altkorn, R. Efficient elimination of fluorescence background from Raman
768 spectra collected in a liquid core optical fiber. *Appl Spectrosc* **54**, 1837–1841 (2000).
- 769 62. Shea, D. A. & Morris, M. D. Bone tissue fluorescence reduction for visible laser Raman
770 spectroscopy. *Appl Spectrosc* **56**, 182–186 (2002).
- 771 63. Macdonald, A. M. & Wyeth, P. On the use of photobleaching to reduce fluorescence
772 background in Raman spectroscopy to improve the reliability of pigment identification on
773 painted textiles. *Journal of Raman Spectroscopy* **37**, 830–835 (2006).
- 774 64. Golcuk, K. *et al.* Is photobleaching necessary for Raman imaging of bone tissue using a
775 green laser? *Biochim Biophys Acta Biomembr* **1758**, 868–873 (2006).
- 776 65. Andreeva, A., Abarova, S., Stoitchkova, K., Picorel, R. & Velitchkova, M. Selective
777 photobleaching of chlorophylls and carotenoids in photosystem I particles under high-light
778 treatment. *Photochem Photobiol* **83**, 1301–1307 (2007).
- 779 66. Bonnier, F. *et al.* Analysis of human skin tissue by Raman microspectroscopy: Dealing with
780 the background. *Vib Spectrosc* **61**, 124–132 (2012).
- 781 67. Tatarkovič, M. *et al.* The minimizing of fluorescence background in Raman optical activity
782 and Raman spectra of human blood plasma. *Anal Bioanal Chem* **407**, 1335–1342 (2015).
- 783 68. Garg, N., Wang, K. & Martin, S. W. A Raman spectroscopic study of the evolution of
784 sulfates and hydroxides in cement-fly ash pastes. *Cem Concr Res* **53**, 91–103 (2013).
- 785 69. Bouchard, M. & Smith, D. C. Catalogue of 45 reference Raman spectra of minerals
786 concerning research in art history or archaeology, especially on corroded metals and
787 coloured glass. *Spectrochim Acta A Mol Biomol Spectrosc* **59**, 2247–2266 (2003).
- 788 70. Choi, S., Lee, S. K., Kim, N. H., Kim, S. & Lee, Y. N. Raman spectroscopy detects
789 amorphous carbon in an enigmatic egg from the Upper Cretaceous Wido Volcanics of South
790 Korea. *Front Earth Sci (Lausanne)* **7**, (2020).
- 791 71. Schito, A., Romano, C., Corrado, S., Grigo, D. & Poe, B. Diagenetic thermal evolution of
792 organic matter by Raman spectroscopy. *Org Geochem* **106**, 57–67 (2017).
- 793 72. Khatibi, S. *et al.* Understanding organic matter heterogeneity and maturation rate by Raman
794 spectroscopy. *Int J Coal Geol* **206**, 46–64 (2019).
- 795 73. Tai, F. C., Wei, C., Chang, S. H. & Chen, W. S. Raman and X-ray diffraction analysis on
796 unburned carbon powder refined from fly ash. *Journal of Raman Spectroscopy* **41**, 933–937
797 (2010).
- 798 74. Guedes, A. *et al.* Characterization of fly ash from a power plant and surroundings by micro-
799 Raman spectroscopy. *Int J Coal Geol* **73**, 359–370 (2008).

- 800 75. Tunstall, L. E., Scherer, G. W. & Prud'homme, R. K. A new hypothesis for air loss in
801 cement systems containing fly ash. *Cem Concr Res* **142**, 106352 (2021).
- 802 76. Potgieter-Vermaak, S. S., Potgieter, J. H., Belleil, M., DeWeerd, F. & Van Grieken, R. The
803 application of Raman spectrometry to the investigation of cement: Part II: A micro-Raman
804 study of OPC, slag and fly ash. *Cem Concr Res* **36**, 663–670 (2006).
- 805 77. Brandt, N. N., Chikishev, A. Y. & Tonevitsky, A. G. Background photobleaching in Raman
806 spectra of aqueous solutions of plant toxins. in *ICONO 2001: Novel Trends in Nonlinear
807 Laser Spectroscopy and Optical Diagnostics and Lasers in Chemistry, Biophysics, and
808 Biomedicine* vol. 4749 349 (SPIE, 2002).
- 809 78. Darvin, M. E., Brandt, N. N. & Lademann, J. Photobleaching as a method of increasing the
810 accuracy in measuring carotenoid concentration in human skin by Raman spectroscopy.
811 *Optics and Spectroscopy (English translation of Optika i Spektroskopiya)* **109**, 205–210
812 (2010).
- 813 79. Wang, H., Zhao, J., Lee, A. M. D., Lui, H. & Zeng, H. Improving skin Raman spectral
814 quality by fluorescence photobleaching. *Photodiagnosis Photodyn Ther* **9**, 299–302 (2012).
- 815 80. Zięba-Palus, J. & Michalska, A. Photobleaching as a useful technique in reducing of
816 fluorescence in Raman spectra of blue automobile paint samples. *Vib Spectrosc* **74**, 6–12
817 (2014).
- 818 81. Dutta, S. B., Krishna, H., Khan, K. M., Gupta, S. & Majumder, S. K. Fluorescence
819 photobleaching of urine for improved signal to noise ratio of the Raman signal – An
820 exploratory study. *Spectrochim Acta A Mol Biomol Spectrosc* **247**, (2021).
- 821 82. Patterson, G. H. & Piston, D. W. Photobleaching in Two-Photon Excitation Microscopy.
822 *Biophys J* **78**, 2159–2162 (2000).
- 823 83. Maher, R. C., Cohen, L. F. & Etchegoin, P. *Single molecule photo-bleaching observed by
824 surface enhanced resonant Raman scattering (SERRS)*. *Chemical Physics Letters* vol. 352
825 www.elsevier.com/locate/cplett (2002).
- 826 84. Deschenes, L. A. & Bout, D. A. Vanden. Single molecule photobleaching: increasing
827 photon yield and survival time through suppression of two-step photolysis. *Chem Phys Lett*
828 **365**, 387–395 (2002).
- 829 85. Ko, D. S. Photobleaching time distribution of a single tetramethylrhodamine molecule in
830 agarose gel. *Journal of Chemical Physics* vol. 120 2530–2531 Preprint at
831 <https://doi.org/10.1063/1.1636726> (2004).
- 832 86. Galloway, C. M., Artur, C., Grand, J. & Le Ru, E. C. Photobleaching of fluorophores on the
833 surface of nanoantennas. *Journal of Physical Chemistry C* **118**, 28820–28830 (2014).
- 834 87. Gupta, R., Darwish, G. H. & Algar, W. R. Complex Photobleaching Behavior of
835 Semiconducting Polymer Dots. *Journal of Physical Chemistry C* **126**, 20960–20974 (2022).
- 836 88. Demchenko, A. P. Photobleaching of organic fluorophores: quantitative characterization,
837 mechanisms, protection*. *Methods Appl Fluoresc* **8**, 22001 (2020).
- 838 89. Gill, R. *Modern Analytical Geochemistry: an introduction to quantitative chemical analysis
839 techniques for Earth, environmental and materials scientists*. (Routledge, 2014).
- 840 90. Toporski, J., Dieing, T. & Hollricher, O. *Confocal Raman Microscopy*. *Springer Series in
841 Surface Sciences* vol. 66 (2018).
- 842 91. Pinzani, M. C. C. *et al.* Direct determination of cadmium speciation in municipal solid waste
843 fly ashes by synchrotron radiation induced μ -x-ray fluorescence and μ -x-ray absorption
844 spectroscopy. *Environ Sci Technol* **36**, 3165–3169 (2002).

- 845 92. Bouchard, M. & Smith, D. C. Catalogue of 45 reference Raman spectra of minerals
846 concerning research in art history or archaeology, especially on corroded metals and
847 coloured glass. in *Spectrochimica Acta - Part A: Molecular and Biomolecular Spectroscopy*
848 vol. 59 2247–2266 (2003).
- 849 93. Sherwin, R., Clark, R. J. H., Lauck, R. & Cardona, M. Effect of isotope substitution and
850 doping on the Raman spectrum of galena (PbS). *Solid State Commun* **134**, 565–570 (2005).
- 851 94. Jozef Struis, R. P. W., Nachtegaal, M., Mattenberger, H. & Ludwig, C. The fate of lead in
852 MSWI-fly ash during heat treatment: An X-ray absorption spectroscopy study. *Adv Eng*
853 *Mater* **11**, 507–512 (2009).
- 854 95. Falgayrac, G., Sobanska, S. & Brémard, C. Heterogeneous microchemistry between CdSO₄
855 and CaCO₃ particles under humidity and liquid water. *J Hazard Mater* **248–249**, 415–423
856 (2013).
- 857 96. Thema, F. T., Beukes, P., Gurib-Fakim, A. & Maaza, M. Green synthesis of Montepelite
858 CdO nanoparticles by *Agathosma betulina* natural extract. *J Alloys Compd* **646**, 1043–1048
859 (2015).
- 860

Supplementary Material

Enhancing Phase Identification in Waste-to-Energy Ashes: Role of Raman Spectroscopy, Background Fluorescence, and Photobleaching

Hamza Samouh, Vikram Kumar, Halle-Mari Santiago, Nishant Garg

Department of Civil and Environmental Engineering, University of Illinois Urbana-Champaign,

Urbana, Illinois, 61801, United States

Table

Table 1. Elemental composition (weight %) of WTE fly ashes from XRF. The ashes are listed by decreasing calcium concentration.

WTE Fly Ash	Ca	Cl	S	Zn	K	Si	Al	Fe	Ti	Br	Pb	Other
1	65.1	20.5	4.8	3.2	1.9	1.3	0.0	0.9	0.4	0.7	0.5	0.6
2	61.8	20.1	5.6	3.8	2.3	1.9	0.0	1.0	0.6	0.8	0.5	1.5
3	61.4	20.3	5.4	3.7	2.4	2.0	1.0	1.1	0.7	0.7	0.5	0.7
4	60.1	24.3	4.8	3.3	1.9	1.3	1.0	0.9	0.4	0.7	0.5	0.6
5	60.1	20.5	5.8	3.8	2.3	2.4	1.1	1.1	0.8	0.7	0.5	0.8
6	55.6	25.4	5.9	4.2	2.1	1.6	1.2	1.1	0.5	0.9	0.6	0.8
7	50.6	26.9	7.9	4.3	3.1	2.5	0.0	1.4	0.9	0.8	0.5	1.1
8	49.3	27.7	7.4	4.3	3.2	2.6	1.1	1.2	0.8	0.7	0.4	1.4
9	47.5	27.7	6.7	4.6	3.0	2.9	2.4	1.4	0.8	0.9	0.6	1.6
10	46.8	28.6	8.8	5.0	2.8	2.4	1.2	1.3	0.7	0.8	0.5	1.0
11	46.7	29.1	7.8	4.4	3.4	2.7	1.2	1.3	0.8	0.7	0.4	1.4
12	46.7	28.8	8.0	4.1	4.3	3.0	0.9	1.3	0.8	0.6	0.4	0.9

Figures

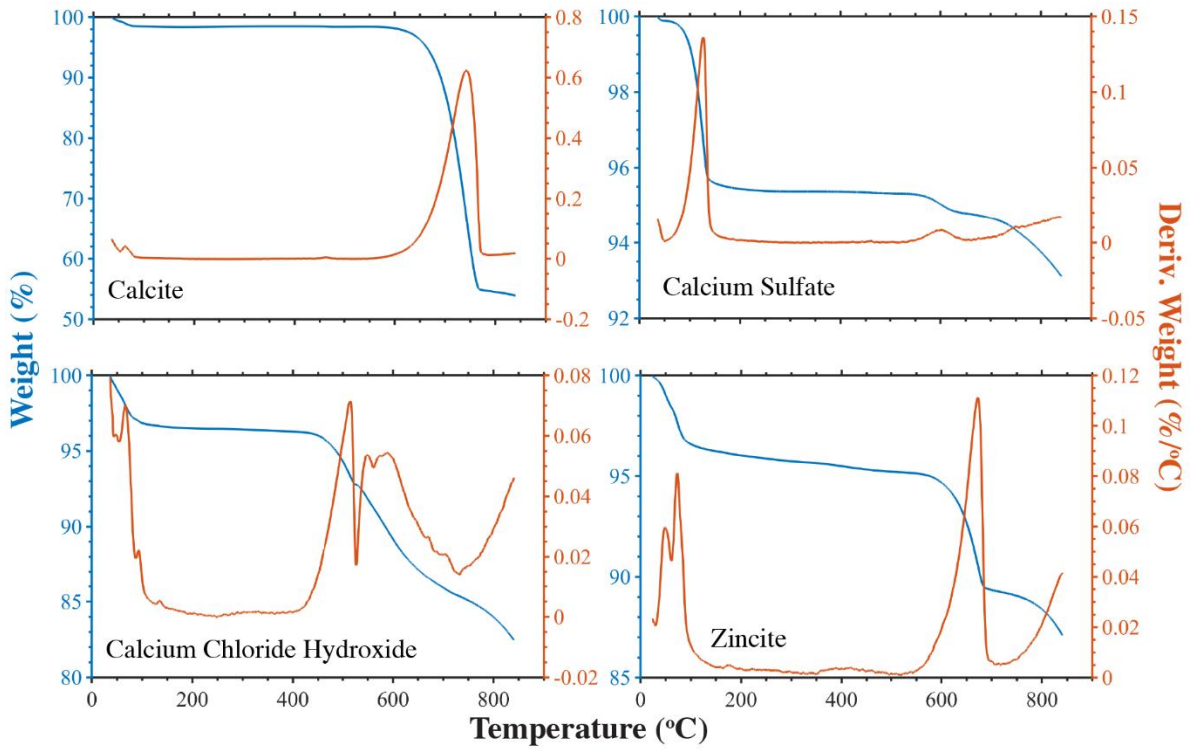


Fig. S1. Thermogravimetric curves for calcite, calcium sulfate, calcium chloride hydroxide, and zincite.

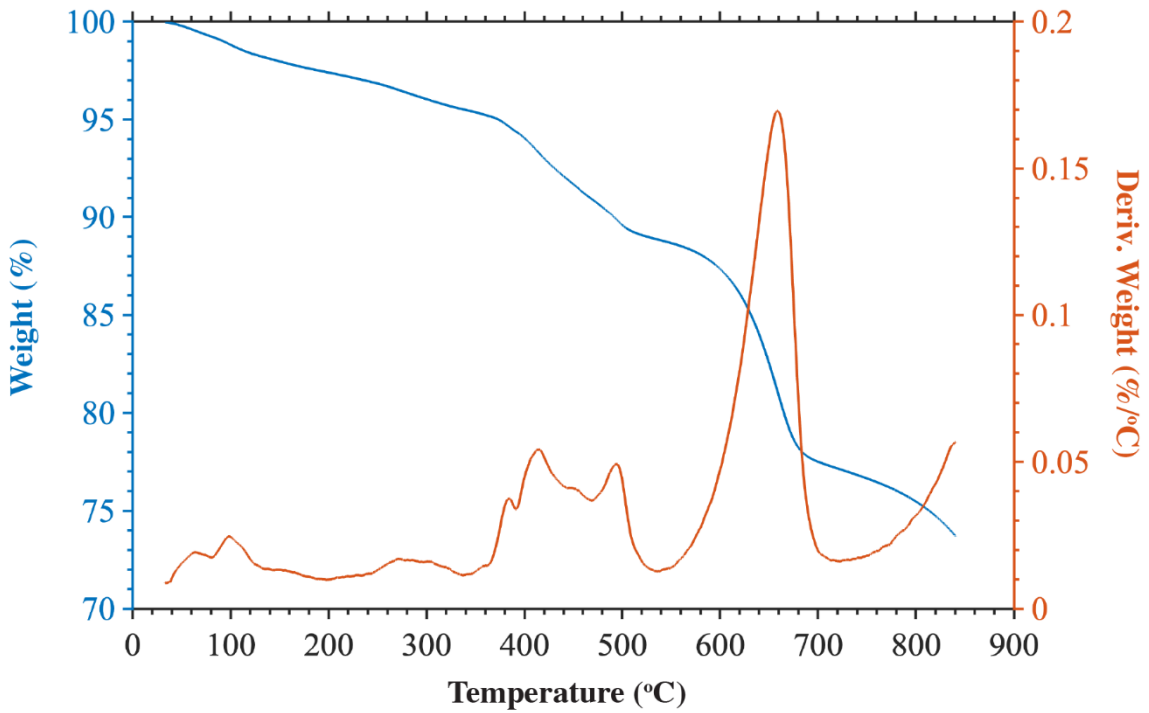


Fig. S2. Thermogravimetric curve for WTE Fly Ash 1.

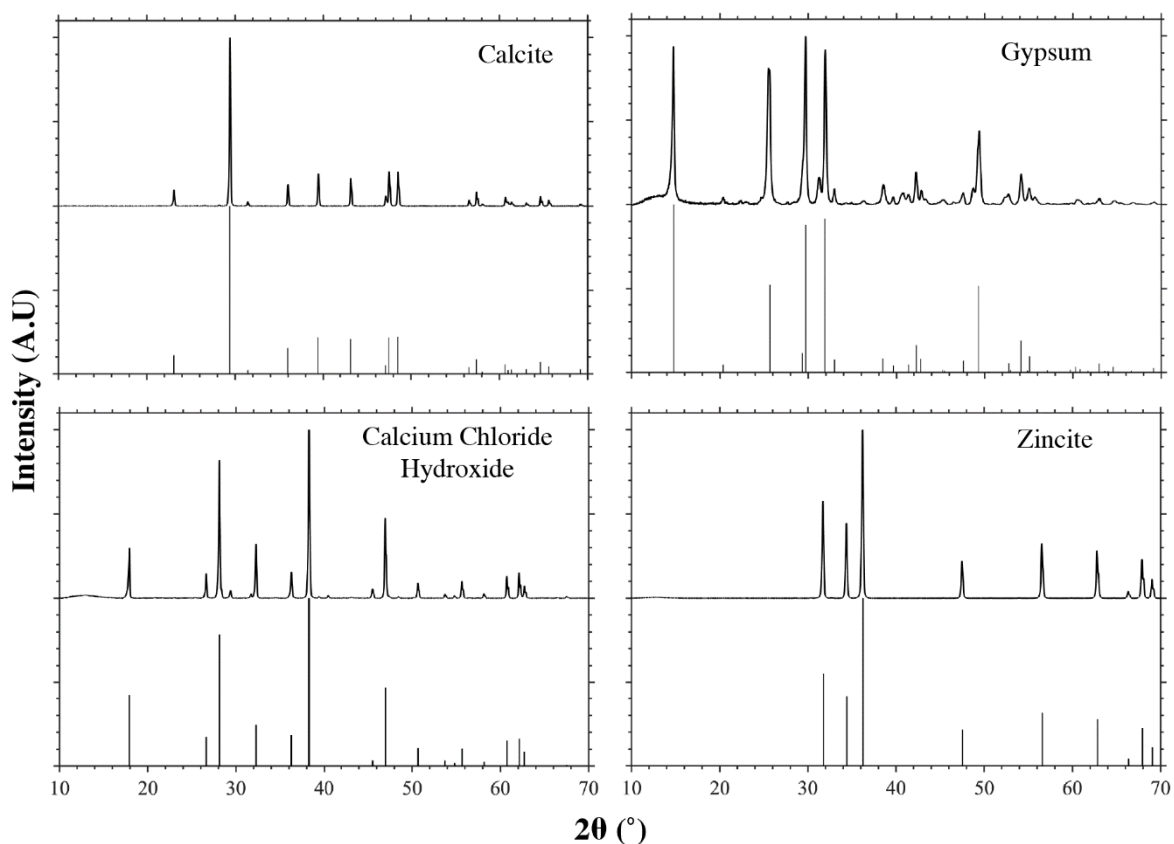


Fig. S3. X-ray powder diffraction patterns of calcite, calcium sulfate (gypsum), calcium chloride hydroxide, and zincite used for evaluating the effect of photobleaching on the Raman spectra. In each subplot, the top pattern represents the diffraction pattern measured in the laboratory, whereas the bottom patterns show standard diffraction patterns from the International Center for Diffraction Data Powder Diffraction File database. The standard PDF diffraction patterns for calcite, calcium sulfate (Gypsum), calcium chloride hydroxide, and zincite are PDF 00-066-0867, PDF 04-007-6682, PDF 04-013-0465, and PDF 04-003-2106, respectively.

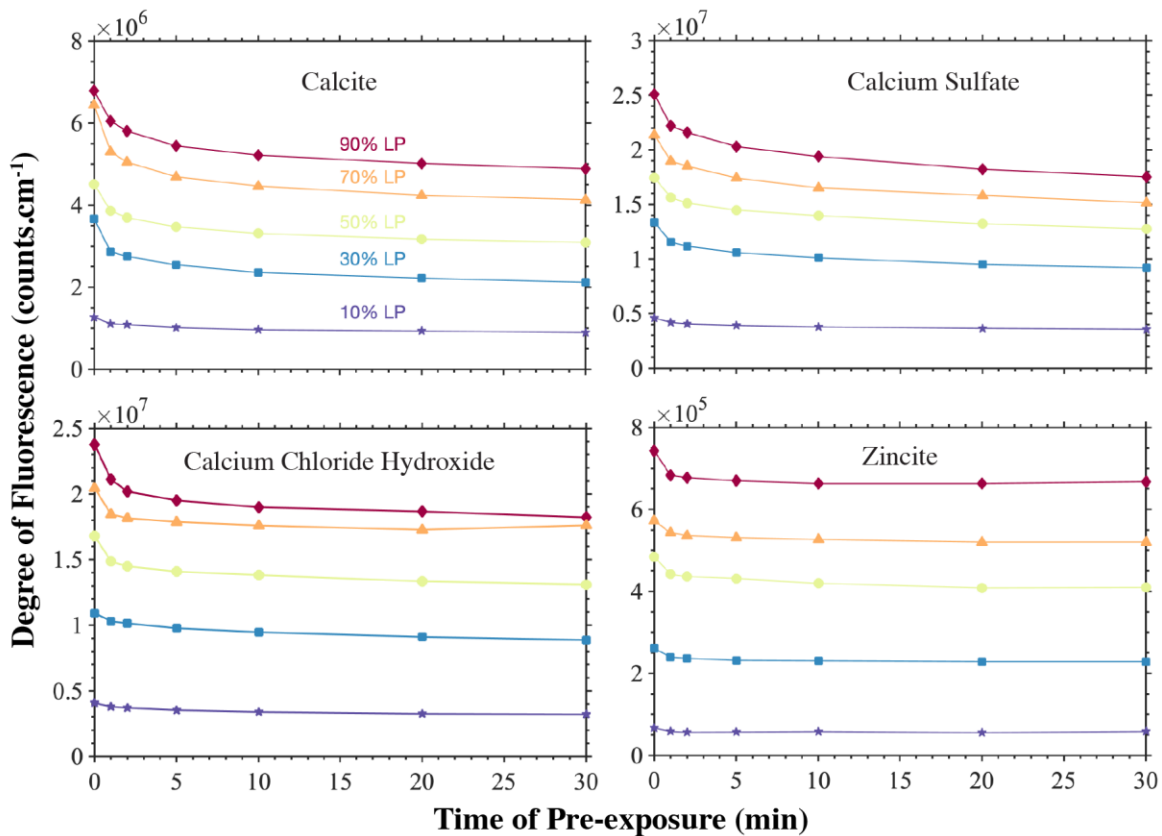


Fig. S4. The effect of photobleaching in reducing fluorescence at different laser powers for calcite, calcium sulfate, calcium chloride hydroxide, and zincite. Degree of fluorescence for calcite, calcium sulfate, calcium chloride hydroxide, and zincite are defined for their most prominent characteristic Raman peaks. The most prominent characteristic Raman peaks for calcite, calcium sulfate, calcium chloride hydroxide, and zincite occur at 1082 cm^{-1} , 1011 cm^{-1} , 669 cm^{-1} , and 435 cm^{-1} .

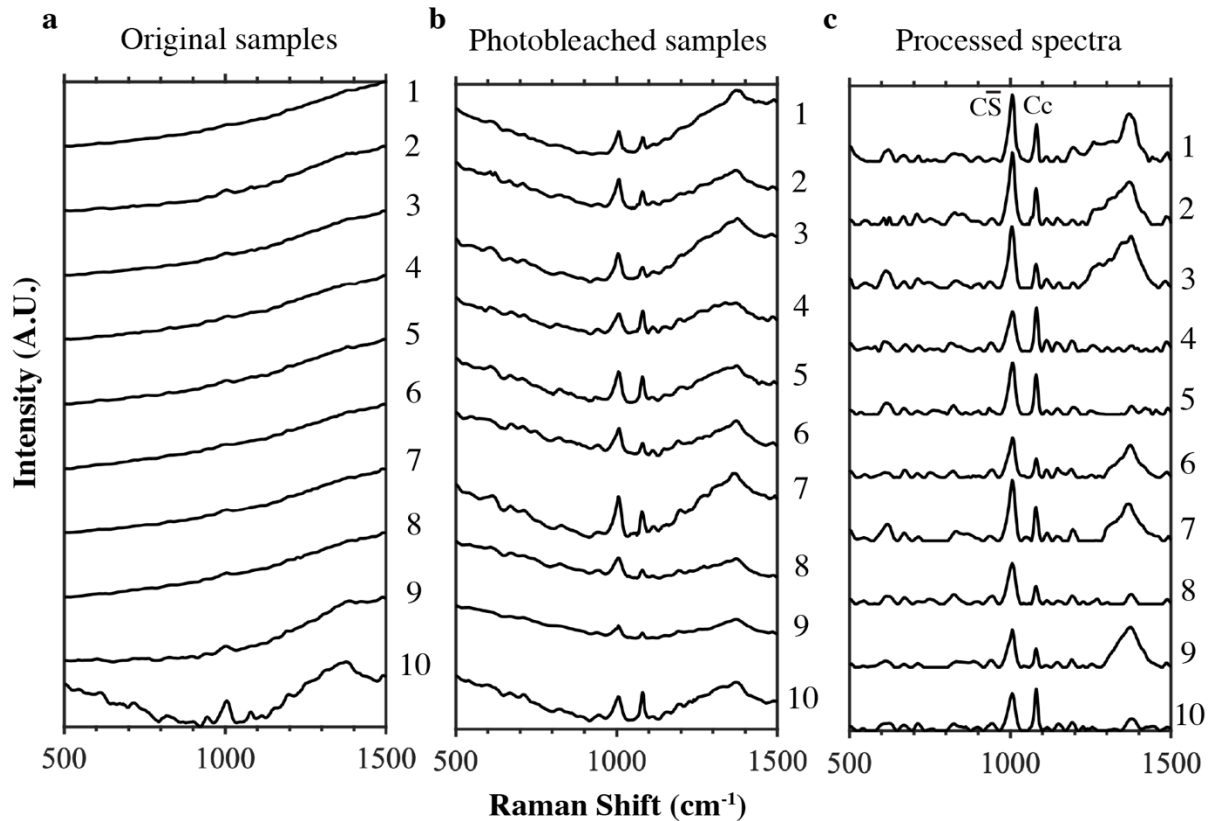


Fig. S5. Raman spectra of WTE fly ash 1 specimen at 10 different spots: (a) Original Raman spectra without photobleaching. (b) Raman spectra after 30 minutes of photobleaching. (c) Raman spectra shown in Figure S5b after noise and background removal. Cc denotes calcite and CS denotes calcium sulfate. All the Raman spectra in this figure were collected with an acquisition time of 6 seconds, and the laser power is fixed at 30% (135 mW).

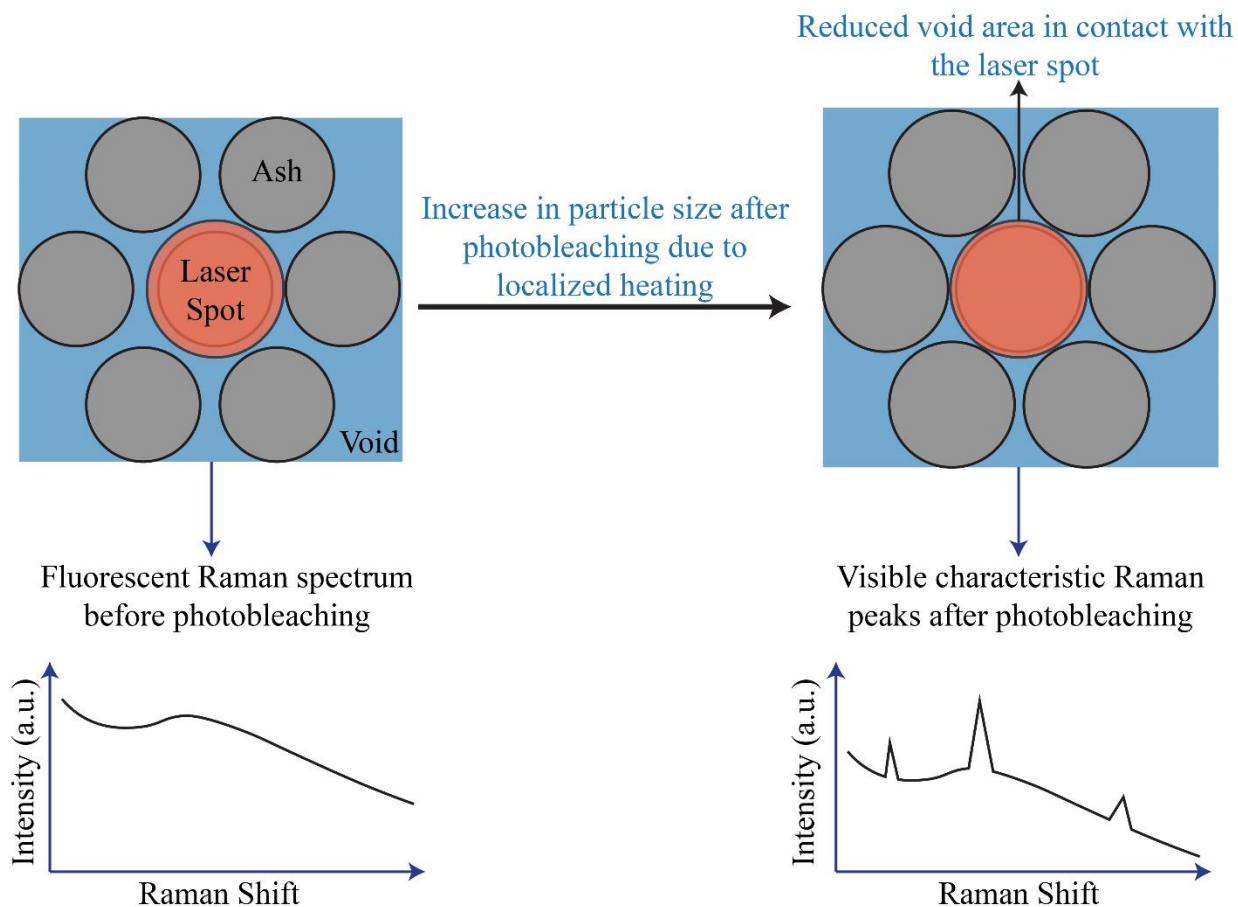


Fig. S6. A schematic illustrating the changes in the morphology of ash particles after photobleaching. The prolonged laser exposure during photobleaching causes localized heating, leading to an increase in particle size. As a result of increased particle size after photobleaching, less void area (porosity) remains in contact with the laser spot, reducing the extent of mismatch between the refractive indices at the void and ash particle interface. The reduction in the mismatch between the refractive indices at the interface results in less laser scattering, reducing the background (fluorescence) in the Raman spectrum of ash particles.

Matlab Code:

This MATLAB code analyzes Raman spectroscopy data from 12 datasets, each representing different Waste-to-Energy (WTE) ashes. The analysis includes data loading, noise removal, background estimation, and background correction. The script loads the data for each dataset and then selects a range of data (based on wavenumbers) for analysis. After that, the script removes noise from the data using a Savitzky-Golay filter, estimates the background signal via preliminary smoothing and piecewise cubic interpolation, and corrects the original signal by subtracting the estimated background. It also identifies valid local minima below the preliminary smoothed background. The processed data is then plotted and saved in three graphs: (1) the original vs. noise-removed spectrum, (2) the noise-removed spectrum vs. estimated background, and (3) the background-corrected spectrum. These graphs are saved as PNG files. Lastly, the script stores the background-corrected spectrum in the cell array for further use.

```
% Load the data for the 12 WTE ashes
datasets = {'FA1830_30', 'FA1833_30', 'FA1834_30', 'FA1835_30', 'FA1836_30', 'FA1837_30', ...
           'FA1838_30', 'FA1840_30', 'FA1841_30', 'FA1842_30', 'FA1844_30', 'FA1846_30'};

wte_ashes = cell(1, length(datasets));

start_wavenumber = 1500; % Enter your desired starting wavenumber here
end_wavenumber = 500; % Enter your desired ending wavenumber here

for i = 1:length(datasets)
    % Load the dataset
    data = load(datasets{i});

    % Get the wavenumbers and intensities
    variable_name = [datasets{i}, '_30']; % Use the correct variable name
    wavenumbers = data.(variable_name)(:, 1);
    intensities = data.(variable_name)(:, 2);

    % Find the indices corresponding to the start and end wavenumbers
    start_index = find(wavenumbers <= start_wavenumber, 1, 'first');
    end_index = find(wavenumbers >= end_wavenumber, 1, 'last');

    % Store the truncated wavenumbers and intensities in the cell array
    wte_ashes{i}.wavenumbers = wavenumbers(start_index:end_index);
    wte_ashes{i}.intensities = intensities(start_index:end_index);
end

num_datasets = length(wte_ashes);

for i = 1:num_datasets
    wavenumbers = wte_ashes{i}.wavenumbers;
    intensities = wte_ashes{i}.intensities;
```

```

% Perform noise removal using Savitzky-Golay filter
frame_length = 9;
poly_order = 2;
noise_removed_intensities = sgolayfilt(intensities, poly_order, frame_length);

% Preliminary smoothing to estimate background
prelim_span = 50; % This should be larger than your expected peak width
prelim_smoothed_intensities = smooth(wavenumbers, noise_removed_intensities, prelim_span, 'loess');

% Find local minima points
[minima, minima_idx] = findpeaks(-noise_removed_intensities);
minima = -minima; % Convert back to positive values

% Use only minima that are below the preliminary smoothed background
valid_minima_idx = minima < prelim_smoothed_intensities(minima_idx);
minima = minima(valid_minima_idx);
minima_idx = minima_idx(valid_minima_idx);

% Perform piecewise cubic interpolation to estimate background
interpolated_background = interp1(wavenumbers(minima_idx), minima, wavenumbers, 'pchip', 'extrap');

% If any point of the interpolated background is above the data, replace it with the data point
interpolated_background = min(interpolated_background, noise_removed_intensities);

% Subtract the interpolated background from the data to get the background-corrected spectrum
background_corrected = noise_removed_intensities - interpolated_background;

% Define vertical shifts for the plots
shift1 = 0.2 * max(intensities);
shift3 = 0.5 * max(noise_removed_intensities);

% Create a new figure for this dataset
figure;

% 1st Plot - Original spectrum and Noise Removed spectrum
subplot(1, 3, 1);
plot(wavenumbers, intensities, 'k', 'DisplayName', 'Original Spectrum');
hold on;
plot(wavenumbers, noise_removed_intensities + shift1, 'b', 'DisplayName', 'Noise Removed Spectrum');
xlabel('Raman Shift (cm-1)');
ylabel('Intensity (a.u.)');
title(['Original Spectrum & Noise Removed Spectrum (' , datasets{i}, ')']);
legend('show');
hold off;
pbaspect([3 2 1]);

% 2nd Plot - Noise removed and Background corrected

```

```

subplot(1, 3, 2);
plot(wavenumbers, noise_removed_intensities, 'k', 'DisplayName', 'Noise Removed Spectrum');
hold on;
plot(wavenumbers, interpolated_background, 'r', 'DisplayName', 'Estimated Background');
xlabel('Raman Shift (cm-1)');
title(['Noise Removed Spectrum & Estimated Background (' , datasets{i}, ')']);
legend('show');
hold off;
pbaspect([3 2 1]);

% 3rd Plot - Background Corrected Spectrum
subplot(1, 3, 3);
plot(wavenumbers, background_corrected, 'k', 'DisplayName', 'Background Corrected Spectrum');
xlabel('Raman Shift (cm-1)');
ylabel('Intensity (a.u.)');
title(['Background Corrected Spectrum (' , datasets{i}, ')']);
legend('show');
pbaspect([3 2 1]);

% Save the figure
saveas(gcf, ['Raman_Spectrum_', datasets{i}, '.png']);

% Store the background-corrected spectrum in the cell array
wte_ashes{i}.background_corrected = background_corrected;

% Full screen
set(gcf, 'Position', get(0, 'Screensize'));

end

```